Hyperfine Interact
DOI 10.1007/s10751-012-0570-2

Application of Mössbauer spectroscopy in magnetism

Werner Keune

Abstract An overview is provided on our recent work that applies ^{57}Fe Mössbauer spectroscopy to specific problems in nanomagnetism. ^{57}Fe conversion electron Mössbauer spectroscopy (CEMS) in conjunction with the ^{57}Fe probe layer technique as well as ^{57}Fe nuclear resonant scattering (NRS) were employed for the study of various nanoscale layered systems: (i) metastable fct-Fe; a strongly enhanced hyperfine magnetic field B_{hf} of $\sim$39 T at 25 K was observed in ultrahigh vacuum (UHV) on uncoated three-monolayers thick epitaxial face-centered tetragonal (fct) ^{57}Fe(110) ultrathin films grown by molecular-beam epitaxy (MBE) on vicinal Pd(110) substrates; this indicates the presence of enhanced Fe local moments, μ_{Fe}, as predicted theoretically; (ii) Fe spin structure; by applying magnetic fields, the Fe spin structure during magnetization reversal in layered (Sm–Co)/Fe exchange spring magnets and in exchange-biased Fe/MnF$_2$ bilayers was proven to be non-collinear and depth-dependent; (iii) ferromagnet/semiconductor interfaces for electrical spin injection; CEMS was used as a diagnostic tool for the investigation of magnetism at the buried interface of Fe electrical contacts on the clean surface of GaAs(001) and GaAs(001)-based spin light-emitting diodes (spin LED) with in-plane or out-of-plane Fe spin orientation; the measured rather large average hyperfine field of $\sim$27 T at 295 K and the distribution of hyperfine magnetic fields, P(B_{hf}), provide evidence for the absence of magnetically "dead" layers and the existence of relatively large Fe moments ($\mu_{Fe} \sim 1.8\ \mu_B$) at the ferromagnet/semiconductor interface. - Finally, a short outlook is given for potential applications of Mössbauer spectroscopy on topical subjects of nanomagnetism/spintronics.

W. Keune (✉)
Fakultät für Physik, Universität Duisburg-Essen, 47048 Duisburg, Germany
e-mail: wernerkeune@web.de

W. Keune
Max-Planck-Institut für Mikrostrukturphysik, Weinberg 2, 06120 Halle, Deutschland

Keywords Mössbauer spectroscopy · CEMS · Nuclear resonance scattering (NRS) · Magnetism · Interfaces · Thin films · Multilayers · Hyperfine field · Spin structure · Exchange spring magnets · Exchanged bias · Iron/gallium arsenide

1 Introduction

Solid state magnetism is a cooperative phenomenon and results from the interaction of atomic magnetic moments that experience magnetic exchange forces, magneto-crystalline anisotropy forces and magnetic dipolar-field forces [1]. Figure 1 displays a schematic listing of some interesting phenomena of solid state magnetism. These encompass the spatial arrangement of magnetic moments (spin structures, such as, e.g., ferromagnetic (F), antiferromagnetic (AF), spin-density-wave (SDW) or spin-glass-type structures), external-field induced magnetic phase transitions [2] and the temperature dependence of the magnetization M(T) or of the hyperfine magnetic field $B_{hf}(T)$ (where the dimensionality of the magnetic system plays a crucial role in the vicinity of the magnetic ordering temperatures [3, 4], T_C or T_N), spin waves and Stoner excitations in metals, magnetization hysteresis loops (along magnetic easy or hard axes, determining magnetic anisotropy), spin-orbit coupling and spin orientations at surfaces/interfaces, and magnetic domain structures. The latter are of crucial important for technological applications, e.g., in magnetic data storage. Magnetically ordered metals are described by a spin-dependent electronic band structure, which shows two bands, the majority (or "spin-up") band and the minority (or "spin down") band. Both bands are shifted in energy relative to each other by the exchange splitting E_{ex}, leading to different electronic density-of-states ($N_\uparrow$ and $N_\downarrow$) at the Fermi energy E_F and, therefore, to an electronic spin polarization P of conduction electrons at E_F. For bcc Fe, the spin polarization at the Fermi energy is $P = 44\%$ [5]. Recently, Heusler compounds with the $L2_1$ crystallographic structure, such as Co_2FeSi, which are potential "half-metallic" ferromagnets with a theoretical spin polarization of 100%, attract high interest because of potential spintronics applications [6].

Two breathtaking discoveries triggered a tremendous upswing of new branches of solid state magnetism, namely nanomagnetism, magnetoelectronics and spintronics [7–11]: the observation of (i) oscillatory interlayer exchange coupling (IEC) by P. Grünberg and coworkers [12], and (ii) giant magnetoresistance (GMR) by A. Fert and coworkers [13] and by P. Grünberg and coworkers [14]. For their findings, A. Fert and P. Grünberg were awarded the Nobel prize in physics in 2007. Figure 2 (top) shows schematically the oscillatory IEC between two ferromagnetic metallic layers separated by a non-magnetic metallic spacer layer [10]. The interlayer exchange-interaction parameter J oscillates as a function of the spacer layer thickness t between ferromagnetic (F) coupling and antiferromagnetic (AF) coupling due to the long-range Ruderman–Kittel–Kasuya–Yoshida (RKKY) interaction mediated by conduction electrons [15]. Figure 2 (bottom) displays the GMR effect: a higher electrical resistance R_{AP} at antiparallel magnetization orientation in the remanent state (at applied field $B_0 = 0$ T) and a lower resistance R_P at parallel orientation at magnetic saturation [10]. The GMR ratio is defined as $(R_{AP} - R_P)/R_P = \Delta R/R_P$. The effect is caused by spin-dependent scattering of conduction electrons at the

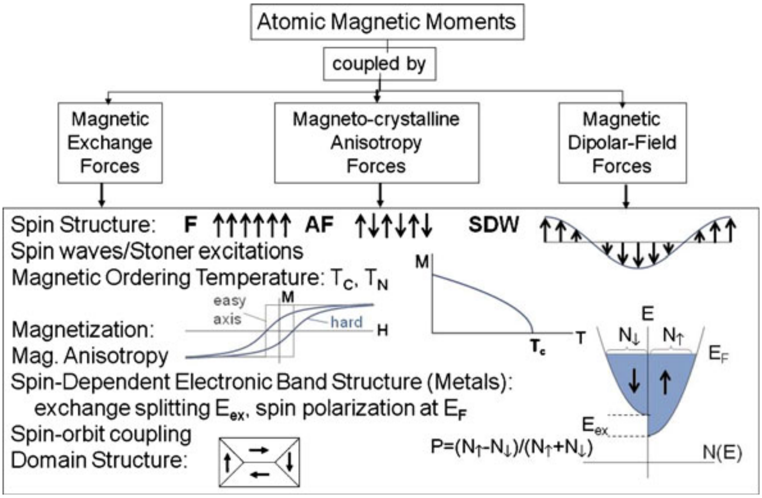

Fig. 1 Schematic representation of some phenomena and topics of interest in solid state magnetism

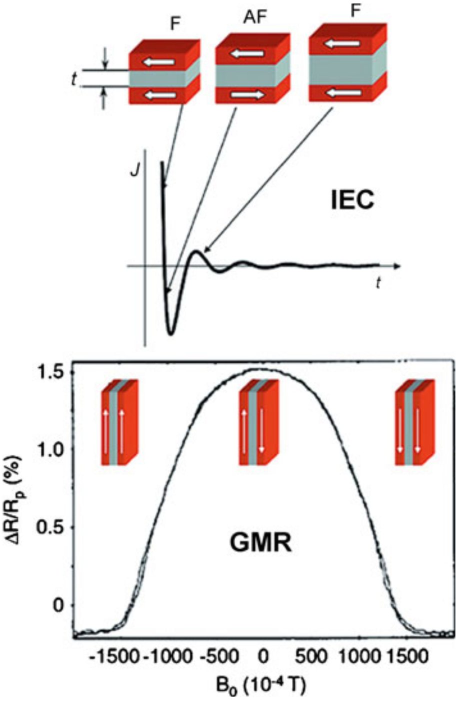

Fig. 2 *Top*: schematics of the indirect oscillatory interlayer exchange coupling J between two ferromagnetic metallic layers separated by a non-magnetic metallic spacer layer of varying thickness t; *bottom*: giant magnetoresistance (GMR) effect $(R_{AP} - R_P)\,R_P = \Delta R/R_p$ versus applied field B_0 (according to Ref. [14]). At remanence, the magnetizations of the two ferromagnetic layers are antiparallel (AP), whereas they are parallel (P) at magnetic saturation. (Adapted from Ref. [10])

Fermi energy [16]. If the non-metallic spacer layer is replaced by an insulating tunnelling layer, one talks about tunnelling magnetoresistance (TMR).

The impact of the Mössbauer effect on solid state magnetism was described in an excellent review article by J. Chappert in 1983 [17]. Since then, applications of

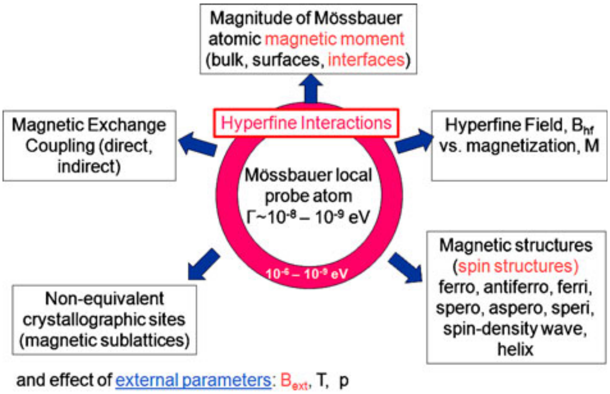

Fig. 3 Schematic representation of some magnetic phenomena that can be studied via magnetic hyperfine interaction by Mössbauer spectroscopy

Mössbauer spectroscopy in magnetism have developed tremendously, partially due to the use of conversion electron Mössbauer spectroscopy (CEMS) for the study of surface/interface magnetism [18–20] and the development of nuclear resonant scattering (NRS) of synchrotron radiation [21]. It is impossible to present a comprehensive review of the impact of Mössbauer spectroscopy on the field of magnetism in a short article. Instead, some representative applications, selected from our own work, will be presented and discussed here.

The Mössbauer nucleus with its nuclear magnetic moment acts as a local probe in the solid. The nuclear and atomic (electronic) magnetic moments are coupled by the magnetic hyperfine interaction (Fig. 3). This means that the nuclear magnetic moment senses a local magnetic field (the hyperfine field B_{hf}) produced by the electrons. The unique feature of the Mössbauer effect is its fantastic energy resolution, which enables to detect the effects of hyperfine interactions on the nuclear energy levels (Fig. 4), which are of the order of 10^{-6} to 10^{-9} eV. The magnitude of the hyperfine field B_{hf} is a rough and indirect measure of the magnitude of the Mössbauer atomic magnetic moment. In this respect, the Mössbauer effect is complementary to other powerful methods, like X-ray magnetic circular dichroism (XMCD) [22], which, however, provides the local atomic magnetic moment directly with high precision, and often enables to distinguish atomic orbital and spin magnetic moments of the electrons. On the other hand, magnetic properties of non-equivalent crystallographic sites (magnetic sublattices) in metallic *alloys*, as revealed by their different hyperfine fields, may be observed by Mössbauer spectroscopy [6, 23, 24], whereas such magnetic sublattices cannot be resolved by XMCD, and only the average atomic magnetic moment is measured by the latter technique [24]. It is well known that the hyperfine field and the Mössbauer isomer shift (chemical shift) both correlate with the chemical charge state of the Mössbauer atom. The best example are high-spin Fe^{2+} and Fe^{3+} valence states, e.g., in magnetite (Fe_3O_4) nanoparticles [25]. X-ray absorption spectroscopy (XAS) is an alternative method, which has been employed successfully to distinguish Fe^{2+} and Fe^{3+} states in Fe_3O_4 nanoparticles even in a liquid matrix (Warland et al., unpublished).

Other important magnetic phenomena that can be investigated by Mössbauer spectroscopy are magnetic exchange coupling (e.g., via modelling the T-dependence of B_{hf}), magnetic moment arrangements (spin structures), and the relation between the hyperfine field and the macroscopic magnetization M. These properties are

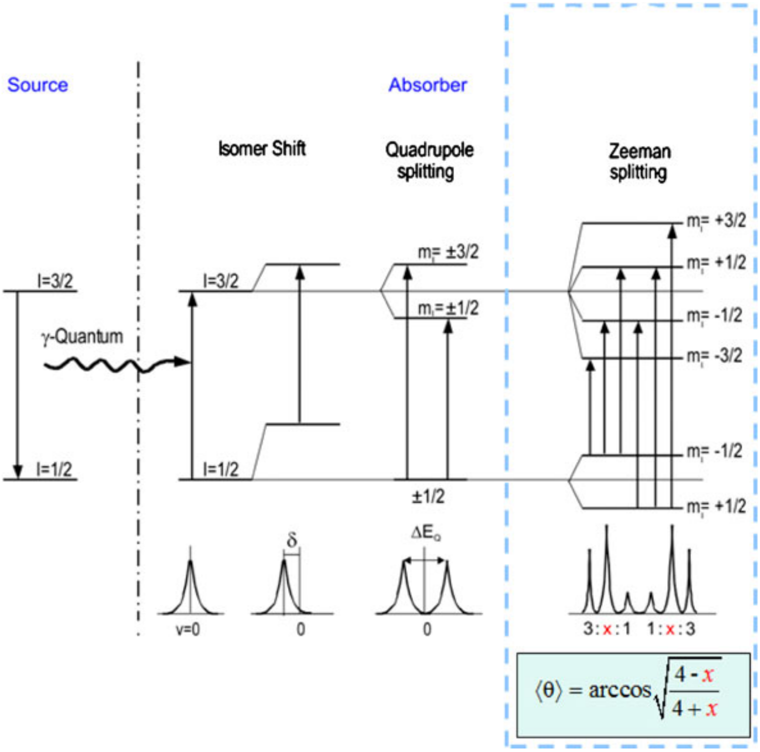

Fig. 4 Effect of different hyperfine interactions (electric monopole, pure electric quadrupole and pure magnetic dipole) on the ^{57}Fe nuclear levels. The relative intensity x (or R_{23}) of lines #2 and 5 of the Zeeman sextet depends on the angle θ between the Fe spin direction (or hyperfine field direction) and the direction of the 14.4-keV γ-ray from the Mössbauer source

often of interest as a function of external parameters (e.g., external field B_{ext}, temperature T or pressure p). For example, the local Fe-selective magnetic hysteresis loop was measured by ^{57}Fe Mössbauer spectroscopy in a strong external magnetic field on nanoscale Fe/Tb multilayers at 5 K, where these samples exhibit hard magnetic properties with a huge coercive field H_c and out-of-plane average Fe spin orientation forming a cone state [26]. The Fe-projected hysteresis loop measured by the Mössbauer effect was found to be remarkably different from the loop obtained by SQUID (superconducting quantum interference device) magnetometry, the latter measuring the macroscopic magnetization of the whole sample [26]. Figure 3 gives a schematic overview of some magnetic phenomena that can be investigated by Mössbauer spectroscopy.

The Mössbauer isotope ^{57}Fe (of ~2% in natural abundance) has found widespread use in the field of magnetism, although ^{119}Sn is a convenient non-magnetic probe for the study of the transferred hyperfine field arising from spin-polarized conduction electrons, e.g., in Cr/Fe multilayers [27] or in Co_2MnSn Heusler alloy films [28, 29]. Figure 4 displays the well-known nuclear level scheme of ^{57}Fe for the different types of hyperfine interactions. They lead to the isomer shift (due to electric monopole interaction), quadrupole splitting (due to electric quadrupole interaction) and Zeeman

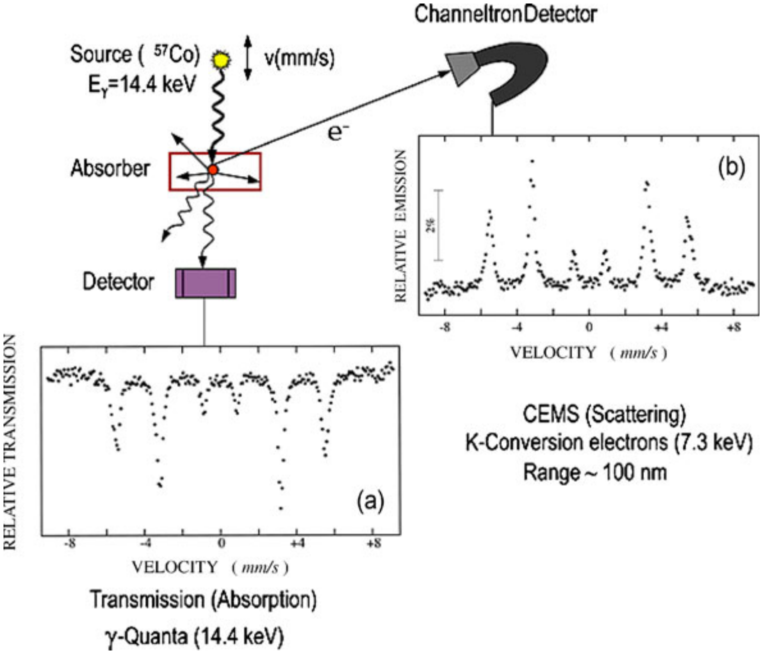

Fig. 5 Schematic setup for ^{57}Fe Mössbauer experiments in **a** transmission geometry or **b** backscattering geometry detecting conversion electrons by use of a channeltron electron detector (CEMS)

splitting (due to Fermi-contact and magnetic dipolar interaction). The latter results in the well-known sextet spectrum, with a line intensity ratio of 3 : x : 1 : 1 : x : 3. From a measurement of the relative line intensity x of the Mössbauer lines number 2 and 5, the average angle $< \theta >$ between the γ-ray direction and the hyperfine-field direction (or Fe spin direction) in the sample can be deduced by use of the expression $< \theta > = \arccos \left[(4 - x) / (4 + x)\right]^{1/2}$. This gives the possibility to provide information on the arrangement of Fe magnetic moments (Fe spin structure) in the sample, in the bulk and thin films as well as at surfaces and buried interfaces. For bulk bcc Fe, the magnitude of the ^{57}Fe hyperfine field is well-known to be 33.0 T at room temperature (RT) or 33.8 T at 4 K [30]. In some bulk Fe alloys, like Y_xFe_{1-x}, the ratio B_{hf}/μ_{Fe} is practically constant at a value of $\sim$15 T/μ_B [31]. This conversion factor can be used in some cases to estimate the atomic magnetic moment of the Mössbauer atom, μ_{Fe}, from the measured B_{hf} value. This works reasonably well in those cases where the core-polarization contribution, B_{core}, to the total hyperfine magnetic field, B_{hf}, dominates over other contributions, as, for instance, the contribution from spin-polarized conduction electrons, B_{ce}, (spin-polarized by magnetic atoms). As an example, let us consider the chemically ordered quasi-Heusler compound Fe_3Si with the $D0_3$ structure, where two inequivalent Fe lattice sites exist [23, 24]: Fe(D) sites with $B_{hf}(D) = 30.8$ T and Fe(A) sites with $B_{hf}(A) = 20$ T, and corresponding Fe atomic moments of $\mu_{Fe}(D) = 2.2\ \mu_B$ and $\mu_{Fe}(A) = 1.35\ \mu_B$, as determined by magnetic neutron scattering [32]. This results in a ratio of 14.0 T/μ_B for the D site and 14.8 T/μ_B for the A site, i.e., in a deviation of $\sim$6%.

The Mössbauer effect can be measured in transmission or backscattering geometry, as shown schematically in Fig. 5. Mössbauer spectra from surfaces, thin films and multilayers are measured effectively by detection of the 7.3-keV conversion electrons which have a mean escape depth from below the Fe surface of ~100 nm [33]. For thin-film preparation in ultrahigh vacuum (UHV) and *in situ* CEMS, a channeltron electron detector can be used, and the sample may be studied *in situ* from low temperature to RT or higher [34]. Due to the small angle of acceptance and low detection efficiency of the channeltron, ^{57}Co Mössbauer sources of high activity (of the order of ~100 mCi or 3.7 GBq) are required for investigations of ultrathin ^{57}Fe films in UHV, occasionally with long measurement times of up to ten days per spectrum.

In the following, selected applications of CEMS and NRS in the field of interface magnetism and thin-film magnetism will be presented.

2 Enhanced hyperfine magnetic field in fct Fe(110) ultrathin films on a vicinal Pd(110) substrate

The structural and hyperfine magnetic properties of epitaxial Fe ultrathin films on the vicinal Pd(110) surface were investigated by means of LEED (low-energy electron diffraction), RHEED (reflection high-energy electron diffraction) and ^{57}Fe CEMS [35].

Earlier experimental work demonstrated that Pd becomes ferromagnetic when in proximity to Fe [36, 37] and carries a magnetic moment [38]. These results were supported by theoretical studies [39, 40]. For interfacial Fe in Fe/Pd multilayers, increased hyperfine fields were discovered by Li et al. [41] using Mössbauer spectroscopy. Cheng et al. [42] measured a strong (14%) enhancement in the magnitude of the hyperfine field, $|B_{hf}|$, of the 2-ML thick interfacial Fe region in magnetron-sputtered Fe/Pd multilayers by extrapolation to low T. By considering only the core polarization of the Fe atomic shell, these authors deduced an Fe atomic moment of 2.8 μ_B from $|B_{hf}|$, being in agreement with theoretical results on Fe/Pd(001) superlattices by Stoeffler et al. [40]. Fe on Pd(001) is the most studied system, experimentally [43, 44] and theoretically [45, 46]. Other substrate orientations, such as Pd(110), have attracted less attention [47].

Our choice of the Fe/vicinal-Pd(110) system was motivated by the fact that the vicinal Pd(110) surface exhibits a large atomic step density and, consequently, shows a strong step-induced in-plane magnetic anisotropy in the Fe overlayer [47]. Knowing that the Fe magnetic moments are oriented in-plane makes the Mössbauer data analysis easier. Furthermore, the induced ferromagnetic moment extends up to ~5 ML into the (110) surface of Pd [48].

Our experiments were performed in an UHV chamber (base pressure $<6 \times 10^{-11}$ mbar) equipped with facilities for LEED, RHEED, Auger spectroscopy, Ar^+ sputtering for surface cleaning and *in situ* CEMS. The Pd(110) substrate had a vicinal angle of 5°. The ^{57}Fe ultrathin films (of 95.5% isotopic enrichment) were deposited on the clean Pd(110) surface at a substrate temperature of 70°C. The film thickness and deposition rate (0.25 Å/min) were controlled by a calibrated quartz-crystal microbalance. Further details on the sample preparation are given in Ref. [35]. After ^{57}Fe film preparation and LEED/RHEED studies the sample was transferred

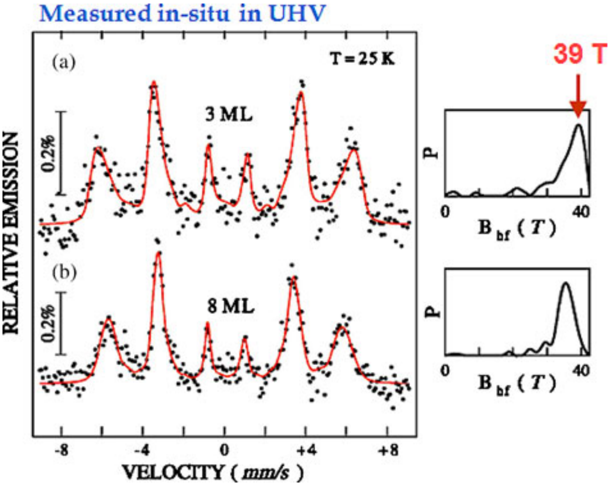

Fig. 6 Mössbauer spectra (CEMS) of **a** 3-ML thick and **b** 8-ML thick epitaxial fct ^{57}Fe(110) ultrathin films on vicinal Pd(110) measured *in situ* in UHV at T = 25 K. The corresponding distribution of hyperfine magnetic fields, $P(B_{hf})$, is shown on the right-hand side. The incident γ-ray was perpendicular to the film surface. (Adapted from Ref. [35])

and fixed in the same UHV system to the cold finger of a liquid-helium flow cryostat. CEMS spectra were taken *in situ* in UHV in zero external field at 25 K (i.e., near thermal magnetic saturation of Fe) using a channeltron electron detector. In order to improve the efficiency of the channeltron, we placed a rectangular-shaped Al tube (with its inner walls coated by a thin MgO film) in front of the channeltron aperture [49]. The MgO layer converts part of the high-energy (7.3 keV) conversion electrons from the sample into low-energy secondary electrons entering the detector. The ^{57}Co(Rh) source of ~40 mCi (or ~1.5 GBq) activity was outside of the UHV system, and the 14.4-keV γ-radiation was transmitted through a UHV-tight Be window in normal incidence to the film plane. LEED and RHEED provided evidence for initial epitaxial (pseudomorphic) ^{57}Fe film growth on Pd(110). The relative in-plane Fe atomic distance (relative to the Pd(110)-substrate atomic distance) perpendicular to the scattering plane has been determined as a function of the ^{57}Fe film thickness from the distance of the RHEED streaks in reciprocal space. This demonstrated the stabilization of the metastable face-centered tetragonal (fct) Fe structure on Pd(110) at small Fe film thickness ($\leq\sim$3 ML Fe) due to the in-plane Fe lattice expansion by the Pd substrate [35]. This lattice expansion was found to be reduced with increasing Fe film thickness. Tetragonal Fe lattice distortions were previously observed by Boeglin et al. [50] during epitaxial growth of Fe on Pd(001) at RT.

The CEM spectra from epitaxial 3 and 8 ML Fe on vicinal Pd(110) recorded at 25 K are shown in Fig. 6a and b, respectively. The spectra were least-squares fitted with a distribution of hyperfine fields $P(B_{hf})$ (right-hand side in Fig. 6), including a small mean electric-quadrupole nuclear level shift ε [51]. This fitting resulted in the following Mössbauer parameters at 25 K: (i) for 3 ML Fe: average hyperfine field $< B_{hf} >= 34.5 \pm 0.4$T, peak in the $P(B_{hf})$ distribution $B_{hf}^{peak} = 39.2 \pm 0.5$T, $2\varepsilon = -0.09 \pm 0.03$mm/s and average angle $< \theta >= 75^\circ \pm 4^\circ$ (relative to the film normal direction); (ii) for 8ML Fe: $< B_{hf} >= 34.2 \pm 0.4$T, $B_{hf}^{peak} = 35.2 \pm 0.5$T, $2\varepsilon = -0.01 \pm 0.02$mm/s and $< \theta >= 90^\circ \pm 5^\circ$. The $< \theta >$ values indicate a preferred in-plane Fe spin orientation, as expected. The other Mössbauer parameters are significantly different from those of bulk bcc Fe (also at 25 K : $B_{hf} = 33.8 \pm 0.2T$, $2\varepsilon = 0 mm/s$). In both Fe/Pd(110) films, the magnitude of the hyperfine field is clearly enhanced relative to that of bulk bcc Fe. For 3 ML Fe/Pd(110), the value of $B_{hf}^{peak} = 39.2T$ is the largest hyperfine field ever observed for Fe films on metallic substrates. The 8-ML Fe/Pd(110) film also exhibits an enhanced hyperfine field (with $B_{hf}^{peak} = 35.2T$), but the enhancement is smaller than that of the 3-ML film.

The electric quadrupole interaction, i.e., the observed nuclear level shift ε, arises from a non-zero electric field gradient (EFG) at the ^{57}Fe nucleus due to an asymmetric (non-spherical) electronic charge distribution around the nucleus. Therefore, the observed (negative) quadrupole level shift 2ε of -0.09 mm/s for the 3-ML Fe/Pd(110) film provides a model-independent proof for a locally non-cubic structure (lattice distortion) of the 3 ML Fe film, in qualitative agreement with our RHEED result [35]. 2ε obtained for the 8 ML Fe film is negligible within error bars, pointing to a much less distorted lattice of this thicker Fe film. One may infer that the change of B_{hf} with changing Fe thickness is the result of the associated structural modification (lattice distortion). This conclusion is supported by the result of Mühlbauer et al. [52], who observed an enhanced Fe atomic moment of 2.7 μ_B by magnetometry, correlated with the fcc Fe structure in polycrystalline Fe/Pd multilayers. A large Fe atomic moment of 2.67 μ_B was also inferred from XMCD measurements on 3 ML Fe/Pd(001) [53].

In this context it is interesting to mention the pioneering depth-selective CEMS studies by Kisters et al. [54], who investigated the interfacial region of Pd-coated epitaxial bcc-Fe(001) film structures using ^{57}Fe probe layers in bcc Fe(001) at different distances from the Pd/bcc-Fe(001) interface. Even at RT B_{hf} was observed to oscillate and to be enhanced to a value of ~37.8 T in the second Fe monolayer below the interface, but approached the bcc-Fe bulk value within 8–10 Fe monolayers. This oscillating behaviour was explained by a superposition of two effects: first, an exponential short-range exchange interaction (mainly due to 3 d–4 d hybridization) within the first three Fe monolayers from the interface, and second an oscillating RKKY-type long-range interaction via conduction electrons in deeper Fe layers. A similar hybridization effect at the fct-Fe/Pd(110) interface may contribute to the strongly enhanced B_{hf} value observed in our work [35].

Is the Fe atomic moment, μ_{Fe}, proportional to the measured hyperfine field B_{hf} at and near the fct-Fe/Pd(110) interface ? In order to address this question we recall that the measured (negative) total hyperfine magnetic field B_{hf} at the ^{57}Fe nucleus in a metal is essentially the sum of several contributions:

$$B_{hf} = B_{int} + B_{dem} = B_{core} + B_{val,core} + B_{val,tr} + B_{dem} = B_{hf,loc} + B_{hf,tr} + B_{dem} \quad (1)$$

The (positive) demagnetizing field B_{dem} is negligible in our case of an in-plane magnetization direction. B_{core} and $B_{val,core}$ are the contributions caused via intra-atomic spin polarization of (1 s, 2 s, 3 s) Fe core electrons and 4 s electrons, respectively, by the local 3 d moment of the Fe Mössbauer atom. $B_{val,tr}$ is the transferred hyperfine field due to inter-atomic polarization of valence 4 s electrons by d electrons of neighboring Fe (and Pd) atoms. According to theory, $B_{hf,loc} = B_{core} + B_{val,core}$ is proportional to the local 3 d moment of Fe [55, 56] ($\mu_{3d} \sim \mu_{Fe}$), whereas $B_{val,tr}$ depends on the degree of hybridization of valence 4 s electrons with d electrons of neighboring atoms surrounding the Mössbauer atom, and on their magnetic moments. Therefore, $B_{val,tr}$ is of nonlocal nature. For the Pd/bcc-Fe(001) system, assuming ideally flat interfaces, S. Handschuh and S. Blügel (private communication) have obtained the monolayer-resolved ground state Fe magnetic moments, μ_{Fe}, and ^{57}Fe hyperfine fields from ab initio full-potential linearized augmented plane wave (FLAPW) calculations. Within an interfacial region of about four atomic layers (layers S, S-1, S-2 and S-3) μ_{Fe} was found to decrease monotonically from an enhanced value of $\sim 2.75\ \mu_B$ (at the Fe "surface" layer S) to $\sim 2.3\ \mu_B$ (at subsurface layer S-1) to the bulk value of $\sim 2.12\ \mu_B$ (at layer S-3). Simultaneously, the magnitude $|B_{hf}|$ behaves nonmonotonically with depth, exhibiting an enhanced value of ~ 35.8 T directly at the Pd/bcc-Fe(001) interface (layer S), an even stronger enhancement to ~ 38.5 T at the first subinterface layer (S-1), followed by a rapid drop to the bulk bcc-Fe value. The computed maximum $|B_{hf}|$ of 38.5 T is in good agreement with our experimental value of $B_{hf}^{peak} = 39.2(5)$ T for 3 ML Fe/Pd(110). The theoretical result (Handschuh and Blügel, private communication) demonstrates that there is no monolayer-resolved proportionality between $|B_{hf}|$ and μ_{Fe}. However, it is remarkable that the theoretical average hyperfine field $<B_{hf}>_{3ML} = 36.2$ T and the theoretical average Fe atomic moment $<\mu_{Fe}>_{3ML} = 2.4\ \mu_B$, both averaged over a 3-ML thick Fe interface region, yield a conversion factor of $15.1\ T/\mu_B$, which agrees surprisingly well with the usual experimental conversion factor of $15\ T/\mu_B$ for bulk bcc-Fe alloys [31]. This observation justifies our conclusion that our measured enhanced hyperfine field $<B_{hf}> = 34.5$ T (averaged over our 3-ML-thick fct-Fe film) corresponds to an enhanced average moment of $<\mu_{Fe}>$ of $\sim 2.3\ \mu_B$. These values of $<B_{hf}> = 34.5$ T and $<\mu_{Fe}> = 2.3\ \mu_B$ should be considered as lower limits, because $P(B_{hf})$ in Fig. 6 shows a low-field tail, which reduces $<B_{hf}>$ and which might be caused by a small fraction of thermally rapidly relaxing Fe spins in the ultrathin films even at 25 K. Finally we like to mention that the bcc structure and the fct structure are related via the so-called Bain transformation [57]. A detailed description of the work presented here is given in Ref. [35].

As mentioned above, $<\theta> = 90°$ for the 8-ML film indicates full in-plane Fe spin orientation. On the other hand, $<\theta> = 75°$ for the 3-ML film reveals a small out of plane Fe spin component. We can speculate about the origin of this perpendicular spin component. It could possibly be induced by the tetragonal lattice distortion of the 3-ML Fe film, resulting in an incomplete quenching of the orbital Fe magnetic moment (as compared to complete quenching in cubic symmetry). Then, the small out-of-plane Fe spin component is induced by spin-orbit interaction. The orbital Fe magnetic moment is expected to be also small. The out-of-plane magnetization component induces a small demagnetizing field along the film normal direction. Assuming a full demagnetizing field B_{dem} of 2 T for Fe, its component along the film-normal direction, $B\perp_{dem} = B_{dem}\cos(75°)$, is 0.5 T only, which is much too small to explain in any way the large B_{hf} enhancement observed here for the 3-ML Fe film.

3 The Fe spin structure in layered systems

As mentioned in the introduction and in Fig. 4, the relative intensity of the sextet lines #2 and 5 depends on the angle θ between the Fe-spin direction (or hyperfine field direction) and the direction of the incoming γ-ray. This offers the exciting

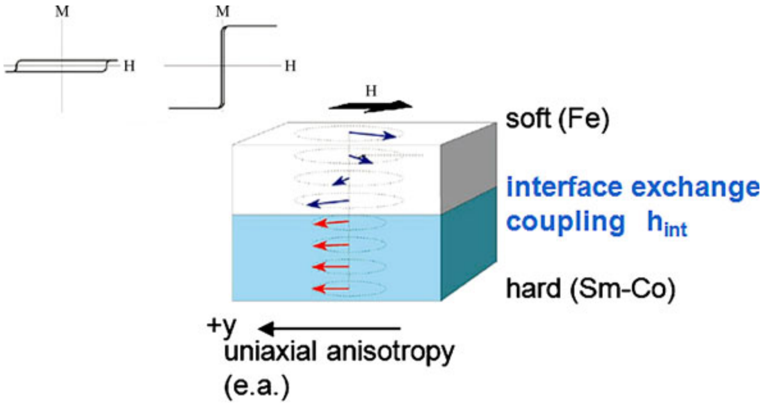

Fig. 7 Schematic representation of a nanoscale exchange-spring magnet, consisting of a magnetically hard ferromagnetic (*bottom*) layer (here: Sm-Co alloy) in contact with a magnetically soft ferromagnetic (*top*) layer (here: bcc Fe). Both layer magnetizations are mutually exchange-coupled at the hard/soft interface. If the soft layer exceeds a certain thickness (the magnetic domain wall thickness), an applied magnetic field H may reversibly induce a helical spin structure in the soft Fe layer during magnetization reversal. (Adapted from Ref. [58])

possibility to determine the Fe spin structure (or Fe spin texture) in the sample by the Mössbauer effect, with or without applying a magnetic field. We have employed ^{57}Fe CEMS with the sample exposed to an in-plane external field H in order to observe changes in the Fe spin structure of layered systems.

3.1 (Sm-Co)/Fe exchange-spring magnets

The first example is the case of a nanoscale (Sm-Co)/Fe exchange spring magnet. The principle of a layered nanoscale exchange spring magnet is illustrated in Fig. 7 [58]. It is a magnetic heterostructure, consisting of a magnetically hard ferromagnetic (bottom) layer (here: Sm-Co alloy) in contact with a magnetically soft ferromagnetic (top) layer (here: bcc Fe). The hard layer is characterized by a low saturation magnetization and a wide hysteresis loop (implying a large coercive field) and possesses a huge in-plane magnetic anisotropy with the easy axis (e.a.) oriented in-plane along the y-axis. The soft layer has a high but narrow hysteresis loop (very small coercive field) and a very small magnetic anisotropy. Both layer magnetizations are mutually exchange coupled at the hard/soft interface, with the interfacial Fe spins strongly pinned to the hard magnet spins. If the soft layer exceeds a certain thickness (the magnetic domain wall thickness, being of the order of a few nanometers), an applied magnetic field H may reversibly induce a helical spin structure in the soft Fe layer. This may occur during magnetization reversal from the magnetically saturated state (originally saturated along the +y-direction) by reversing H along the -y-direction. The resulting helical (sometimes called “twisted”) Fe spin structure resembles the spin configuration in a magnetic domain wall. It can be controlled by an external magnetic field. Such magnetic-field controlled non-collinear spin structures are of relevance in the field of nanomagnetism/spintronics. For example, domain wall motion induced by electrical currents [11, 59] in ferromagnetic nanowires is connected with the movement of non-collinear spin structures along a nanowire.

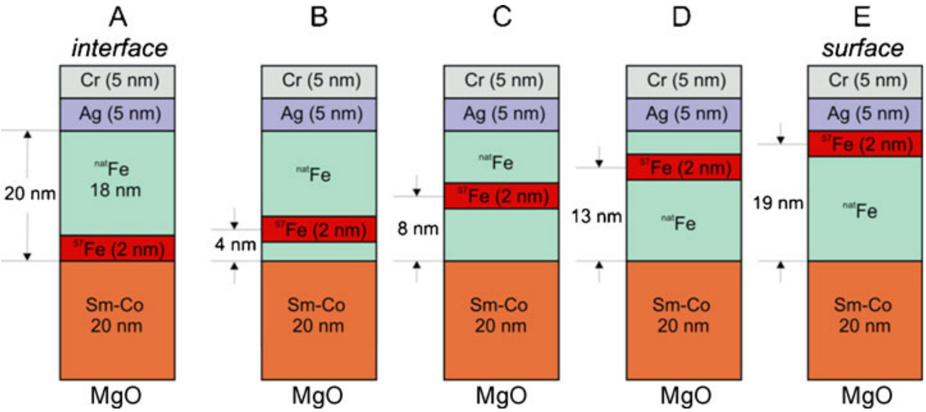

Fig. 8 Schematic representation (cross-sections) of the five different layered (Sm-Co)/Fe exchange-spring samples studied by CEMS. The total thickness of the Sm-Co layer and the Fe layer is 20 nm each. 2-nm thick ^{57}Fe probe layers are placed at different distances d from the (Sm-Co)/Fe interface in the Fe layers. Sample A (interface sample): directly at the interface, d = 1 nm; sample B: d = 4 nm; sample C: d = 8 nm; sample D: d = 13 nm; and sample E (surface sample): d = 19 nm [65]

In the future, this effect may lead to a new type of magnetic memory ("racetrack memory" [11]).

Although ^{57}Fe nuclear resonant scattering [60, 61] and CEMS [62] have been used in the past to elucidate the helical spin structure in exchange spring systems, its determination at the atomic scale is still a challenging problem. For example, in Ref. [62] it was assumed in the model used that the pitch of the Fe spin helix is uniform along the film normal direction, which, very likely, is only a rough approximation. Here, the results of CEMS measurements on (Sm-Co)/Fe bilayers performed at RT in an in-plane external magnetic field will be described. Thin ^{57}Fe probe layers were placed in the Fe layer at different distances from the (Sm-Co)/Fe interface to obtain site-selective (isotope-selective) data during the magnetization reversal process.

Five different (Sm-Co)/Fe bilayer samples with in-plane uniaxial magnetic anisotropy were prepared using dc magnetron sputtering. Details of the preparation are described in Refs. [63] and [64]. Epitaxial Sm-Co layers (20 nm thick) with a nominal composition of Sm_2Co_7 were grown at 600°C on MgO(110) substrates with an epitaxial Cr(211) buffer layer. The epitaxial relationship for the magnetically hard (Sm-Co)(1–100) layer is (Sm-Co)[0001]//Cr[01-1]//MgO[001]. This induces a uniaxial in-plane easy axis parallel to the (in-plane) hexagonal Sm-Co c-axis. In all samples the polycrystalline bcc Fe layer (20 nm in total thickness, of 2.14% in natural isotopic ^{57}Fe abundance) was deposited onto the Sm-Co layer by sputtering at a substrate temperature T_s of 300–400°C. The Fe layer was coated by 5 nm of Ag followed by 5 nm of Cr for protection. Within every Fe layer, a 2-nm thick isotopically enriched ^{57}Fe probe layer (enriched to 95% in ^{57}Fe) was placed by sputter deposition at different distances from the hard/soft interface in order to probe the depth-dependence of the Fe spin structure. This resulted in five different samples labeled samples A (interface sample), B, C, D and E (surface sample) (Fig. 8). The macroscopic magnetic properties of the samples at RT were measured by alternating-gradient magnetometry (AGM). The hysteresis loop shapes observed (not shown)

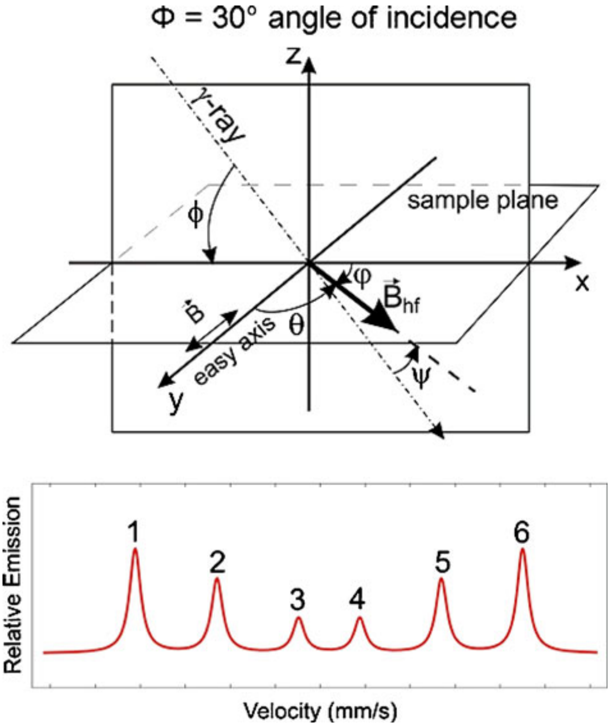

Fig. 9 *Top*: schematic geometrical arrangement of the CEMS measurement at inclined incidence of the γ-ray relative to the sample plane (xy plane). The angle of incidence is $\Phi = 30°$. The external magnetic field H is applied along the Sm-Co easy-axis direction (the y axis). The hyperfine field B_{hf} and Fe atomic magnetic moment μ_{Fe} lie in the sample plane. Ψ is the angle between the γ-ray direction and the direction of B_{hf}. (The angle Ψ is identical to the angle θ in Section 1 and in Fig. 4). The x axis is defined by the projection of the γ-ray direction onto the sample plane. *Bottom*: schematic Zeeman sextet of ^{57}Fe with numbers labelling the six Mössbauer lines

displayed a double step typical for layered exchange-spring magnetic systems [66–68]. Separate switching transitions were observed for the soft Fe and hard Sm-Co layers upon magnetization reversal. As expected, the shape of the hysteresis loops was found to be similar for all five samples in the low- and medium-field range (~ -350 mT $\leq \mu_0 H \leq\sim +350$ mT), where the Fe magnetization reverses, since chemically and magnetically the Fe layers have the same total thickness of 20 nm in all samples.

For detection of conversion electrons, each sample was mounted inside of a small self-built He-4% CH_4 proportional counter. The counter was placed between the poles of an electromagnet with its field H oriented in the sample plane along the easy axis direction (y-direction) of the magnetically hard Sm-Co film. The Fe spin configuration in the ^{57}Fe probe layers during the magnetization reversal process was studied at RT by CEMS in decreasing magnetic fields H, ranging from +1150 mT (+y direction, start) to −1150 mT (−y direction, stop). If the direction of the hyperfine magnetic field at the ^{57}Fe nucleus B_{hf} (which is antiparallel to the direction of the Fe atomic moment, μ_{Fe}) forms an angle Ψ with the incident Mössbauer γ-ray direction (Fig. 9), then the intensity ratio $R_{23} = I_2/I_3 = I_5/I_4$ of lines #2 and 3 (or lines #5 and 4) is given by [69, 70] $R_{23} = 4\left\langle \sin^2(\Psi)\right\rangle / \left[1 + \left\langle \cos^2(\Psi)\right\rangle\right]$, where the brackets <...> indicate averaging over the angular Fe spin distribution in the sample. (The angle Ψ used here is identical to the angle θ used in Section 1 and in Fig. 4). For the case of in-plane distributed Fe magnetic moments and perpendicular γ-ray incidence, i.e., for $\Psi = \Phi = 90°$ in Fig. 9, the intensity ratio is $R_{23} = 4$ and is insensitive to the in-plane

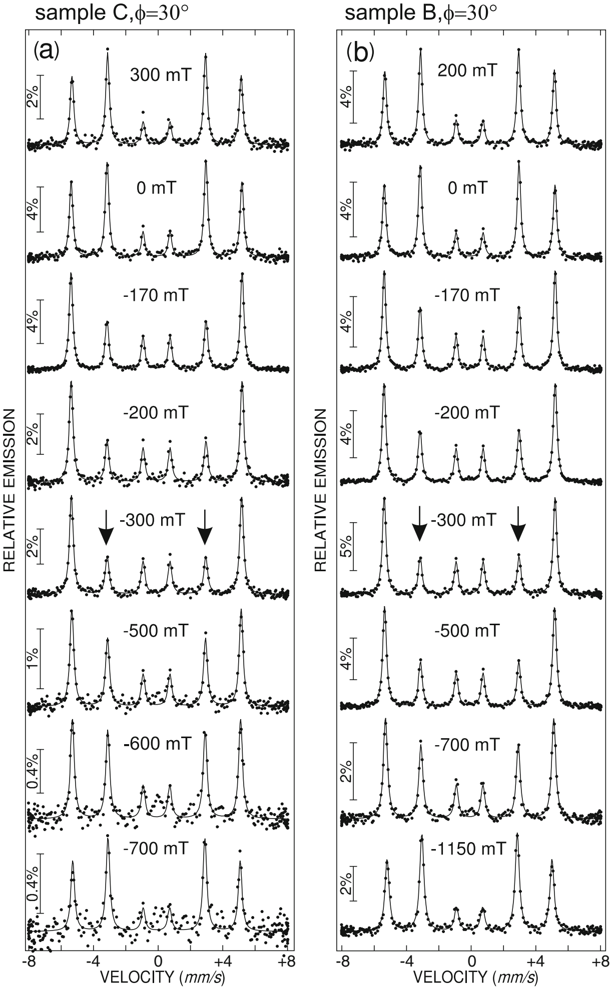

Fig. 10 RT CEM spectra of **a** sample C and **b** sample B, taken at inclined incidence of the γ-radiation (at $\Phi = 30°$) and in different in-plane magnetic fields μ_0H applied along the easy axis direction of the Sm-Co film (along the y direction). For each sample, the sequence of measurements started with the highest (positive) field and finished with the lowest (negative) field. The least-squares fitted curves are explained in the text (Khrenov 2005, unpublished)

spin direction. (This is valid for unpolarized γ-radiation and is applicable here, since we use a ~50 mCi unpolarized ^{57}Co(Rh) source in our experiments). Therefore, the in-plane Fe spin configuration in our sample can be studied only at inclined incidence of the γ-radiation. In our present experiments we have chosen $\Phi = 30° \pm 5°$ as the angle of incidence. From the equation above, the model-independent average quantity

$$\left\langle \cos^2(\Psi) \right\rangle = (4 - \mathrm{R}_{23}) / (4 + \mathrm{R}_{23}) \tag{2}$$

that characterizes the angular distribution of the Fe spins can be obtained from a measurement of the intensity ratio R_{23}.

Typical RT CEM spectra taken under $\Phi = 30°$ and in different applied fields are shown in Fig. 10a and b for sample C and B respectively. The spectra of the other samples (not shown) are of similar quality. For every sample the spectra were measured in the sequence from the highest (positive) field to the lowest (negative)

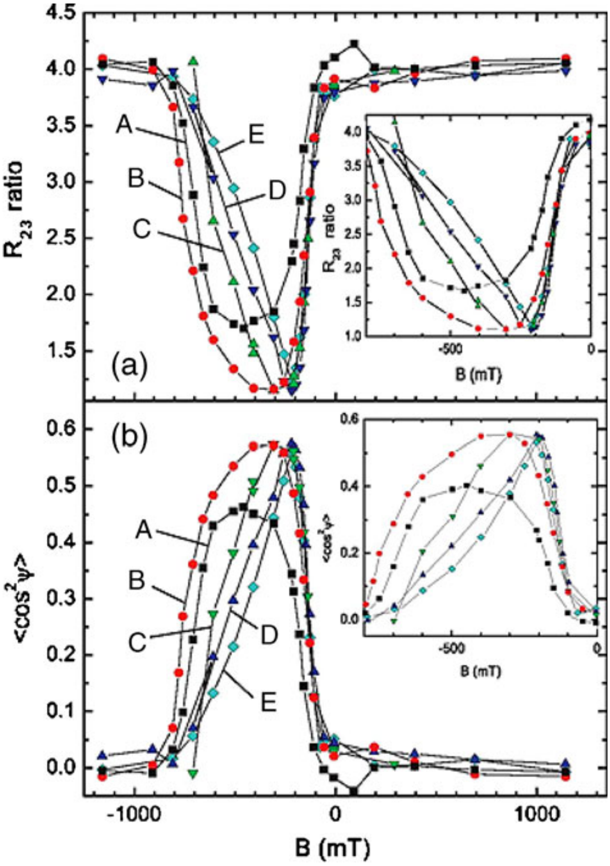

Fig. 11 **a** Measured Mössbauer line intensity ratio R_{23} versus the external field $\mu_0 H = B$ applied along the easy axis direction and following the decreasing field branch of the hysteresis loop, obtained from least-squares fitting of the CEM spectra of samples A to E. *Black squares*: sample A(interface); *red circles*: sample B; *green triangles tip up*: sample C; *dark-blue triangles tip down*: sample D; *light-blue diamonds*: sample E (surface). Insert: zoom of the *left curves*. **b** The model independent average angular quantity $<\cos^2(\Psi)>$ versus the external field $\mu_0 H = B$ obtained from **a**. Symbols in the same color as in **a** are used in **b**. Insert: zoom of the *left curves*. (The lines are a guide for the eye) (Khrenov 2005, unpublished)

field, as indicated in Fig. 10. All spectra in Fig. 10 are simple Zeeman sextets typical for α-Fe, as expected for the ^{57}Fe probe layers sandwiched with natural α-Fe layers on both sides. These spectra were least-squares fitted by one sextet with narrow Lorentzian lines using the program NORMOS by Brand [71]. The magnitude of the hyperfine field B_{hf} obtained for the spectra at remanence (i.e., at $\mu_0 H = 0$ T) is in good agreement with the value of 33.0 T of bulk α-Fe at RT. Obviously, our Fe films consist of the α-Fe phase, as expected. The interesting effect in Fig. 10 is the systematic intensity variation of the lines #2 and 5 (marked by arrows) versus the applied field H. This observation is an atomistic manifestation of the Fe spin reversal process.

The measured line intensity ratio R_{23} and the corresponding angular quantity $<\cos^2(\Psi)>$ versus the in-plane external field $\mu_0 H$ is shown in Fig. 11a and b, respectively, for samples A to E. At magnetic saturation, i.e., for the strongest positive (+1150 mT) and negative (−1150 mT) fields, $R_{23} \sim 4$ and $<\cos^2(\Psi)> \sim 0$, indicating that, for all samples, all the Fe spins point along the applied field direction (along the +y or −y direction, respectively), forming an angle $\Psi = 90°$ with the incident γ-ray. Moreover, the data in Fig. 11 show a nonmonotonic behaviour, i.e., for all samples they show a minimum in $R_{23}(H)$ at (R_{min}, $\mu_0 H_{min}$) and a maximum in $<\cos^2(\Psi)>$ versus μ_0H. When R_{min} (or the maximum, $<\cos^2(\Psi)>_{max}$) is reached at μ_0H_{min}, the Fe spins in the ^{57}Fe probe layer have acquired such a particular in-plane angular spin distribution or Fe spin texture that, in the average, they have a maximum component along the direction of the in-plane projection of the incoming γ-ray, i.e., along the x axis (Fig. 9). This is that particular field where the average Fe spin direction reverses its y-component from positive to negative.

The striking effect in Fig. 11 is that the H-dependences of R_{23} and of $<\cos^2(\Psi)>$ have a different functional behaviour for the different samples A to E, which is a manifestation of the depth-dependence of the Fe spin structure. For example, for sample E (where the ^{57}Fe probe layer is at the "surface" of the natural Fe layer) the field μ_0H_{min} is at a smaller negative μ_0H value than for the interface-sample A (where the probe layer is directly at the hard/soft interface). This tells us that, upon increasing the negative field, the "surface" Fe spins (sample E) switch first, and the interface Fe spins (sample A) switch later due to the stronger coupling of interface Fe spins with the spins of the hard layer. It is also interesting to see that the value of R_{min} (and also of $<\cos^2(\Psi)>_{max}$) is different for the interface sample A (with $R_{min} = 1.7$) and for the off-interface samples B - E (with $R_{min} = 1.2$). This proves that the Fe spin texture upon switching is different for the interface and off-interface samples. It turns out that the depth-dependent Fe spin structure in these samples is rather complex. Presently, efforts are undertaken to determine the Fe spin structure in our samples by simulations using the electronic band-structure theory by Uzdin and Vega [72, 73] with a minimum of assumptions.

3.2 Exchange-biased Fe/MnF_2 bilayers

Exchange coupling at the interface between films of a ferromagnet (F) and an antiferromagnet (AF) is often manifested by a center shift of the magnetic hysteresis loop away from the zero-field axis [74]. This is called the exchange-bias (EB) effect. It is generally conceived that the EB effect originates from the exchange interaction of interfacial F spins and a fraction of interfacial AF spins that are rigidly frozen after field cooling (or after cooling in the remanent state) from a temperature $T > T_N$ (T_N = Néel temperature) to a sufficiently low temperature $T < T_N$. In a simplified picture, if the EB state is induced, for instance, by a positive cooling field, an excess negative applied field is required upon magnetization reversal in order to overcome the pinning of F spins by the interfacial exchange coupling to the frozen AF spins. This then leads to a hysteresis loop shifted towards negative applied fields.

An example of a shifted hysteresis loop is shown in Fig. 12 for an exchange-biased Fe/$FeSn_2$(001) bilayer, measured by SQUID (superconducting quantum interference device) magnetometry at T = 10 K after cooling the sample in a field of 0.5 T [75]. The sample was essentially a Fe/$FeSn_2$(001) bilayer on a clean InSb(001) substrate, where Fe is the F layer and $FeSn_2$ is the AF layer (T_N = 378 K). The exact sample composition was

$$\mathrm{Sn(2nm)/Fe(6nm)/{}^{57}FeSn_2(5nm)/FeSn_2(15nm)/InSb(001)},$$

with the sample coated by 2 nm of Sn for protection. The $FeSn_2$(001) film was epitaxially grown in UHV at T_s = 150°C by co-deposition of natural Fe and Sn, followed by $^{57}FeSn_2$(001) (95% enriched in ^{57}Fe). The subsequent polycrystalline natural Fe film and the Sn film (coating) were grown at RT. Details of Fe/$FeSn_2$

Fig. 12 Magnetic hysteresis loop of an exchange-biased Fe/$FeSn_2$(001) bilayer measured at 10 K after cooling in a field of $\mu_0 H = 0.5$ T. The center of the loop shows a shift by $H_e = -82$ Oe relative to the vertical $H = 0$ axis. H_e is the exchange-bias field. The cooling field and the measurement field were oriented in the film plane along the [108] direction of the epitaxial $FeSn_2$(001) film [75]

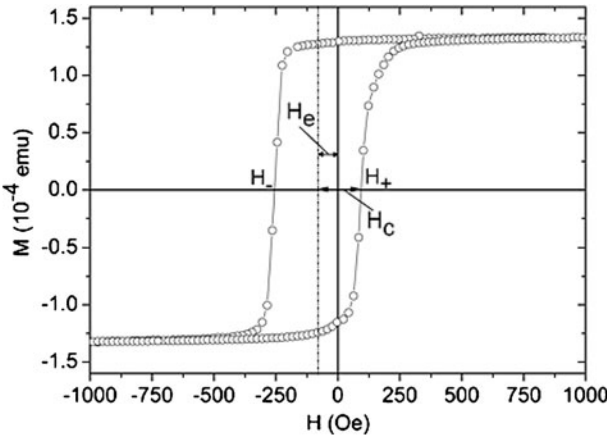

sample preparation are described elsewhere [76–78]. After field-cooling, the center of the hysteresis loop in Fig. 12 shows a clear shift by $H_e = -82$ Oe towards negative fields. The exchange field H_e is a measure of the exchange coupling at the F/AF interface.

The EB effect has found important applications in spin-valve-type devices [79]. Although the EB effect has led to great technological advancement and intense research efforts, investigation of the magnetic structure at the F/AF interface and its depth dependence perpendicular to the film plane (z direction) is a challenging task. For example, some theoretical models predict a helical AF spin structure along the z direction in the F/AF interfacial region upon magnetization reversal [80–82]. Non-collinear spin structures in the F layer (partial domain walls) near the F/AF interface were also theoretically predicted [83, 84] and rarely investigated experimentally [85]. Earlier CEMS studies using ^{57}Fe probe layers at different depths in the Fe layer of exchange-biased Fe/MnF_2 bilayers did not reveal a depth-dependent Fe spin structure in Fe [86, 87]. However, these CEMS measurements were performed at remanence due to the difficulties with electron detection in strong applied fields.

A particular promising technique for the direct measurement of Fe spin structures at surfaces and buried interfaces at low T and in strong external fields is ^{57}Fe nuclear resonant scattering (NRS) of synchrotron radiation, in combination with ^{57}Fe probe layers (a few Ångstroms thick). Using this technique, the depth-dependent Fe spin rotation upon magnetization reversal was measured in exchange-coupled Fe/MnF_2(110) bilayers with an ^{57}Fe probe layer placed at different depths within an ^{56}Fe film (depleted in ^{57}Fe) [88]. MnF_2 is an AF with $T_N = 67$ K. Kiwi et al. [84] proposed a model for exchange-biased Fe/FeF_2(110), where the AF FeF_2 is isostructural with MnF_2. This model predicted that upon magnetization reversal by an applied field, EB energy is reversibly stored in the Fe layer like in an exchange-spring magnet, forming an incomplete magnetic domain wall in the Fe layer [84]. As a consequence of the interfacial F/AF exchange coupling strength $J_{F/AF}$ (being the only adjustable parameter in the calculations), two features in the calculated M-versus-H plot (Fig. 13b) can be noticed: a negative EB field H_e and an asymmetric shape of the M-versus-H plot, marked by "offset" in Fig. 13b. Both features have been confirmed experimentally for Fe/MnF_2, as will be shown below.

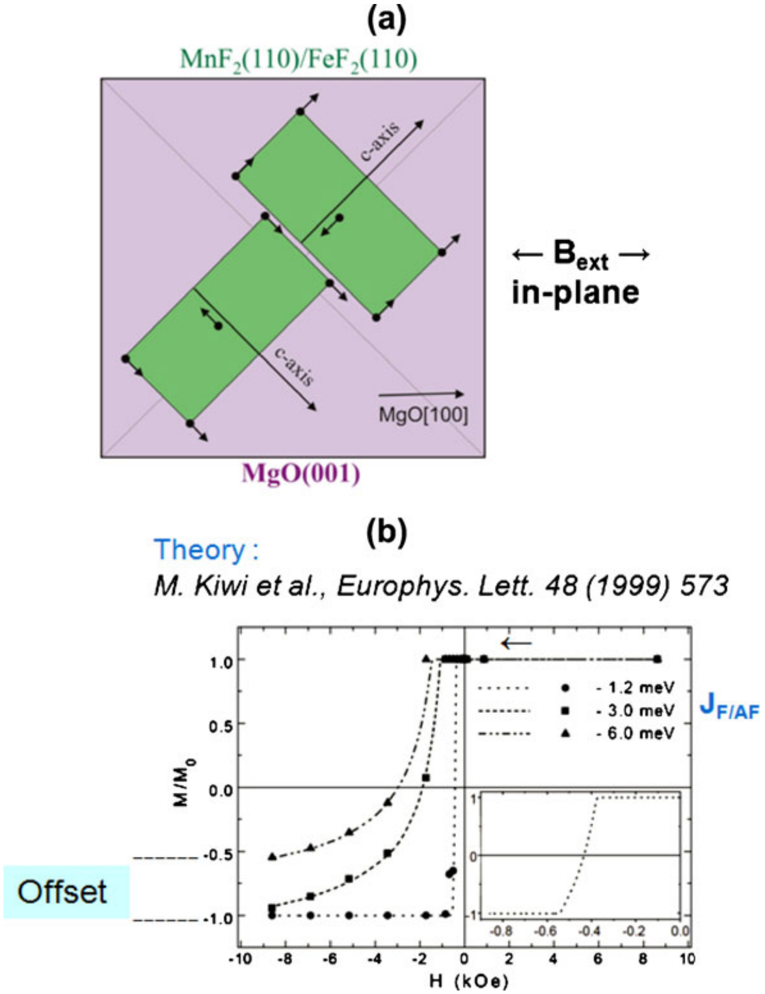

Fig. 13 **a** schematic representation of the AF spin structure in crystallographically twinned MnF_2(110) and FeF_2(110) thin films; the AF easy axes (c axes) are at ±45° relative to the MgO[98] direction (or x axis), along which the magnetic field H and the x-ray beam were aligned. **b** Magnetization M versus applied field H upon magnetization reversal in the exchange-biased state of a Fe/FeF_2 bilayer, computed by Kiwi et al. [84] as a function of the interfacial exchange coupling strength $J_{F/AF}$. The exchange-bias field H_e and the asymmetric shape of the plot depend strongly on $J_{F/AF}$. The asymmetric shape (indicated by "offset") is due to the formation of a non-collinear spin structure (an incomplete domain wall) in the Fe layer. Insert: zoom of the stepped curve near H = 0 kOe. (Adapted from Ref. [84])

The Fe/MnF_2(110) sample structure is shown in Fig. 14a. First an epitaxial 52-nm-thick MnF_2(110) layer was grown by MBE on a MgO(001) substrate carrying a 16-nm-thick ZnF_2(110) buffer layer. The MnF_2 film grows as a (110)-oriented pseudo-twinned quasiepitaxial layer (Fig. 13a) and exhibits a nominally "compensated" AF surface with the Mn spins in the surface plane. Figure 13a also illustrates that the AF easy axes directions (or c-axes directions) of the MnF_2(110) twin domains

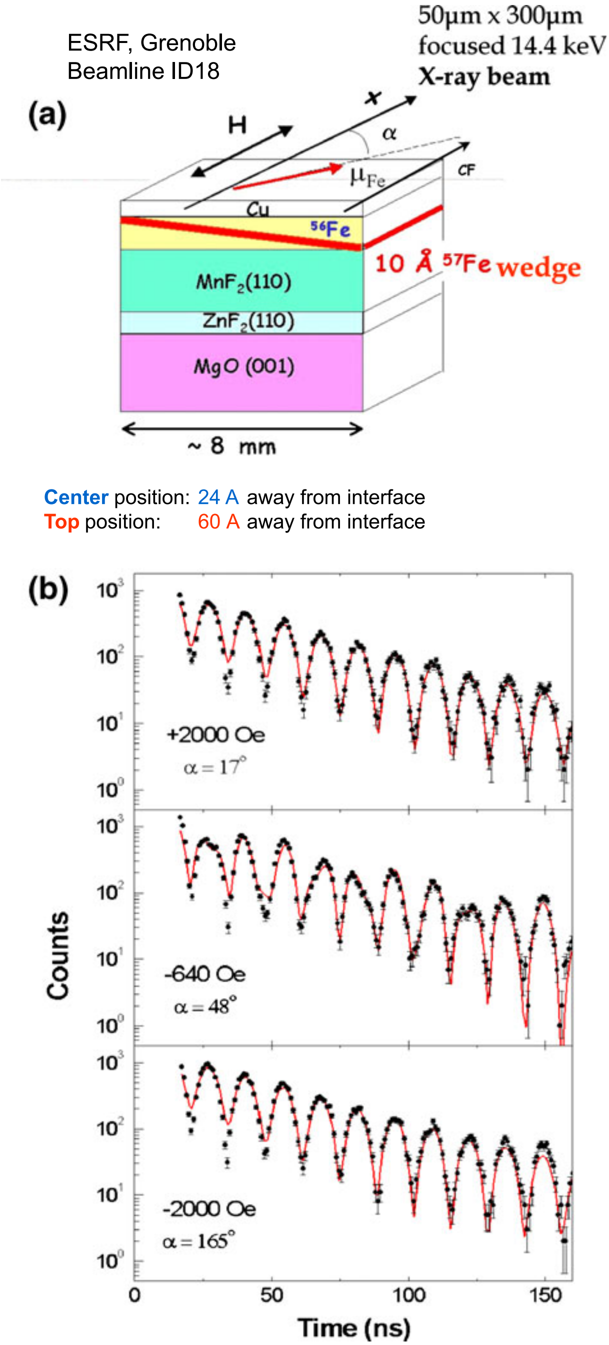

Fig. 14 **a** Schematic diagram of the wedge sample and the NRS experimental geometry: the incident x-ray beam, reflected at an angle of 4 mrad relative to the surface, is oriented along the x direction (the MgO[98] direction), together with the applied field H; (all the arrows are in the sample plane). **b** Typical NRS time spectra measured at 10 K in decreasing magnetic fields, with the x-ray beam probing the ^{57}Fe center position of the wedge. The red solid lines are least-squares fits to the experimental data. α is the angle between the in-plane Fe spin direction and the +x direction (Adapted from Ref. [88])

are oriented at ±45° with respect to the (horizontal) MgO [98] direction (or x axis direction), along which the in-plane magnetic field $B_{ext} = \mu_0 H$ was applied. The 1-nm-thick ^{57}Fe probe layer (95.5% enriched) was inserted diagonally, i.e., between two inverted wedge-shaped ^{56}Fe layers (depleted in ^{57}Fe), providing a polycrystalline Fe layer of 7 nm in total thickness. The sample was capped by 4 nm of Cu.

The NRS experiments were performed at beamline ID18 of the European Synchrotron Radiation Facility (ESRF) in Grenoble, France. The photon beam, at grazing incidence of 4 mrad, was oriented along the MgO [001] direction (or x direction, Fig. 14a) and parallel to the applied field. The experimental arrangement (cryomagnet cryostat) allowed the precise scanning of the photon beam (of 50 μm × 300 μm cross section) over the sample surface. This provides the depth selectivity along the wedge with the ^{57}Fe probe layer at different distances from the F/AF interface. Two beam positions were selected for the NRS measurements: the “center position (2.4 nm away from the F/AF interface) and the “top” position (6.0 nm away from the interface).

In NRS, the time response of the forward scattered intensity reflected from the ultrathin ^{57}Fe probe layer is measured. Some typical time spectra, when the photon beam hits the center position of the wedge, are shown in Fig. 14b. Spectra of similar quality were obtained with the beam at the top position of the wedge. The spectra were taken at 10 K along the decreasing-field branch of the hysteresis loop after field cooling from 150 K in a field of 2 kOe. The measured data were least-squares fitted using the CONUSS program [89] (red solid lines in Fig. 14b). The orientation of the in-plane Fe magnetic moments, μ_{Fe}, with respect to the incident photon-beam direction (x axis), characterized by the in-plane angle α, was determined from the fittings. This provides similar information as obtained from the line intensity ratio R_{23} in conventional Mössbauer spectroscopy, but with higher angular accuracy. A hyperfine field of $B_{hf} = 34.1 \pm 0.2\,T$ at 10 K was obtained for all time spectra at the center and top positions in the entire external field range. Within error bars, this is the expected B_{hf} value for bcc Fe at 10 K. Under the assumption of a unidirectional collinear Fe spin structure within the thin ^{57}Fe probe layer depth sensed by the photon beam, the in-plane angle α was determined as a function of the applied field H. Since NRS of the linearly polarized x-rays used here are unable to distinguish μ_{Fe} components along positive (along + x) or negative (along −x) H directions, respectively, the sign of the SQUID magnetization loop (not shown) was used to determine the magnetization reversal points from the +x to the −x direction.

Following this procedure, a NRS angular hysteresis loop with α versus H can be deduced from the measured data. Figure 15a shows the full 10-K angular hysteresis loop for the ^{57}Fe “center” position of the wedge (2.4 nm away from the interface, full blue circles) and the 10-K descending field branch for the ^{57}Fe “top” position of the wedge (6.0 nm away from the interface, full red squares). For the top position, we notice that the (in-plane) ^{57}Fe spins first rotate continuously and only weakly from full alignment ($\alpha = 0°$) along H = +2000 Oe to an off-field direction with $\alpha = 42°$, and subsequently “jump” unexpectedly to $\alpha = 138°$ followed by a gradual rotation to $\alpha = 180°$ (full alignment) at H = −2000 Oe. The corresponding model Fe spin configuration within the top ^{57}Fe probe layer (angle α) and the directional spin “jump” are sketched in Fig. 15b (based also on earlier CEMS studies on similar samples [86]). Similarly, a jump of the ^{57}Fe spin direction is observed during the descending-field branch as well as during the increasing-field branch for the ^{57}Fe center position (full blue circles, Fig. 15a). It is remarkable that NRS was able to identify the α values between which the ^{57}Fe atomic magnetic moments, μ_{Fe}, jump upon magnetization reversal ! It is striking that the α values observed near the

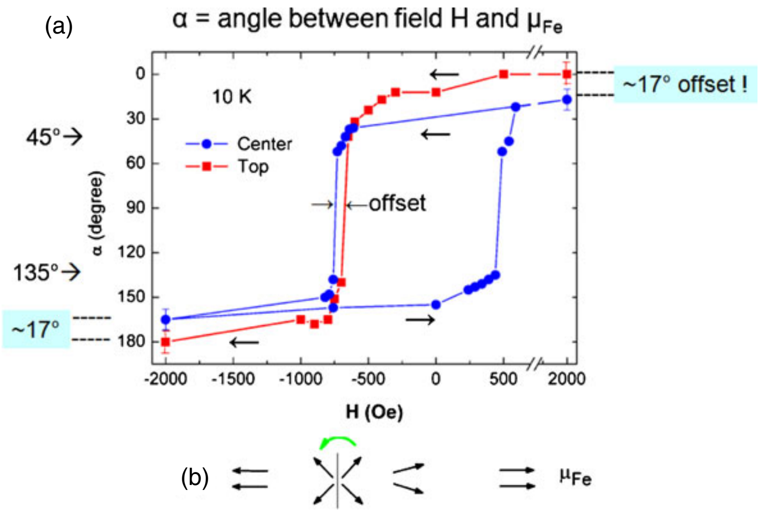

Fig. 15 *Top*: NRS angular hysteresis loop of α versus H measured at 10 K at the ^{57}Fe center position of the wedge (2.4 nm away from the Fe/MnF_2 interface, *blue full circles*) and the descending-field branch of α versus H (at 10 K) at the ^{57}Fe *top position* of the wedge (6.0 nm away from the Fe/MnF_2 interface, *red full squares*). The *center* and *top* data were measured in two independent NRS runs after field-cooling in +2000 Oe from 150 to 10 K. The error bars of α near the reversal are ±3°. *Bottom* or **b**: Schematical model of the Fe spin configuration within the *top* ^{57}Fe probe layer, indicating the directional Fe spin "jump" from $\alpha = 45°$ to $\alpha = 135°$ upon magnetization reversal. (Adapted from Ref. [88])

magnetization reversals are close to the AF easy axes directions (45° and 135°) of the MnF_2 twin domains (Fig. 13a). Thus, the jumps occur from one of the twinned MnF_2 easy axis (±45°) to the other (±135°). This is the result of the strong interfacial exchange coupling, enforcing the Fe spin directions along (or maybe perpendicular to) the AF easy axes. The Fe spins revers by jumps of $\Delta\alpha = 90°$, indicating an angular instability range for the Fe spins exchange coupled to Mn spins of the twinned MnF_2 domains. This is also a direct observation of the four-fold magnetic anisotropy induced by the exchange interaction between the Fe and $MnF_2(110)$ layers.

Figure 15a provides a proof of depth-dependent magnetization reversal at 10 K. This manufests itself in two features: (i) The top-position ^{57}Fe spins of the wedge (6.0 nm away from the F/AF interface) revert earlier (by ~40 Oe) than the ^{57}Fe spins at the center position of the wedge (2.4 nm away from the interface), implying stronger pinning of Fe spins closer to the exchange-biased Fe/MnF_2 interface and, consequently, a depth-dependence of the induced four-fold magnetic anisotropy; (ii) at H = +2000 Oe, the top-position ^{57}Fe spins are fully aligned along the field H ($\alpha = 0°$), whereas the ^{57}Fe spins at the center position are misaligned with respect to the H direction by $\delta\alpha \sim 17°$ (offset). The same tendency is observed at H = −2000 Oe. Thus, the reversal and the saturation are easier to achieve at 6.0 nm that at 2.4 nm from the F/AF interface. Both observations imply that the Fe spin rotation in an exchange-biased system occurs like in a spring magnet, forming a non-collinear spin structure (or partial domain wall), as predicted by Kiwi et al. [84] (Fig. 13b). A more detailed presentation of the work described here can be found in Ref. [88].

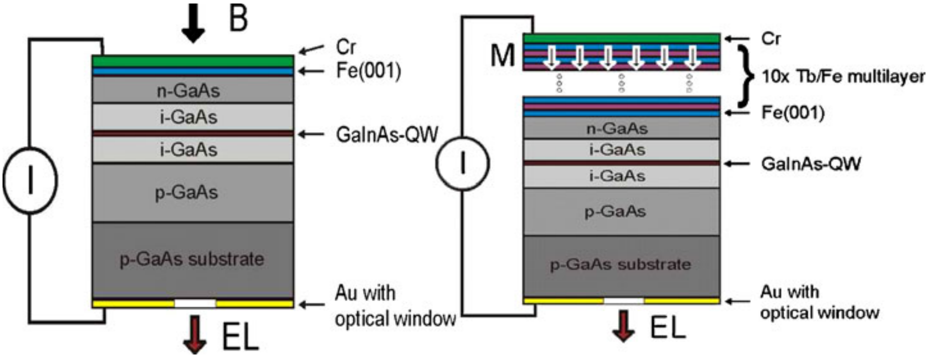

Fig. 16 *Left*: Schematic sketch of the structure of a spin LED with an epitaxial ferromagnetic Fe(001) electrical contact on top and a Au contact at the bottom. The *vertical direction* of the strong magnetic field B and the circular-polarized electroluminescent light (EL) is also indicated. The EL light is emitted from the GaInAs quantum-well after recombination of spin-polarized electrons and unpolarized holes. *Right*: Same as on left-hand side, but with a Tb/Fe multilayer-contact with perpendicular (*vertical*) magnetization at remanence (at B = 0 T) on top. (Adapted from Ref. [97])

4 Ferromagnet/semiconductor heterostructures: Fe on GaAs(001)

Fe/GaAs-based hybrid systems are interesting candidates among metallic ferromagnet (F)/semiconductor (SC) heterostructures that open possible future spintronics applications [90–93], including electrical electron spin injection into the semiconductor [94–98]. A new branch of spintronics, so-called spin-optoelectronics, is developing rapidly [93, 99, 100]. Detection of electrical spin injection into semiconductors has been achieved by exploiting the circular polarization of the electroluminescence (EL) light (of wavelength 855 nm) that is emitted from so-called spin light-emitting diodes (spin LEDs), which are GaAs-based semiconductor heterostructures carrying an electrical ferromagnetic thin-film metal contact (e.g., an epitaxial Fe(001) thin film, the top electrode in Fig. 16 (left)). The EL circular-polarized light is emitted after applying a bias voltage between the top (e.g., Fe) electrode and the bottom (e.g., Au) electrode. The spin-polarized electrons are injected from the ferromagnetic (top) electrode into the semiconductor and move to the quantum-well (QW) of the LED, where they recombine with unpolarized holes under EL light emission [97]. The condition for purely circular-polarized light emission is that the spins of the injected electrons are perpendicular to the QW plane. This follows from optical selection rules [101] based on angular momentum conservation, and from the existence of an orbital angular momentum oriented perpendicular to the quantum well due to electron confinement. Since simple conventional ferromagnetic thin films (like Fe) exhibit in-plane magnetization due to their magnetic shape anisotropy, strong external fields of up to a few Tesla are required to rotate the film magnetization into the perpendicular (vertical) direction. Such high fields are hardly acceptable for future spin-optoelectronics devices, such as spin vertical-cavity surface emitting lasers (VCSELs) [102, 103]. Therefore, the development of more complex ferromagnetic spin-injector contacts with spontaneous out-of-plane magnetization is a key issue for the development of spin-optoelectronic devices. This issue will be discussed later.

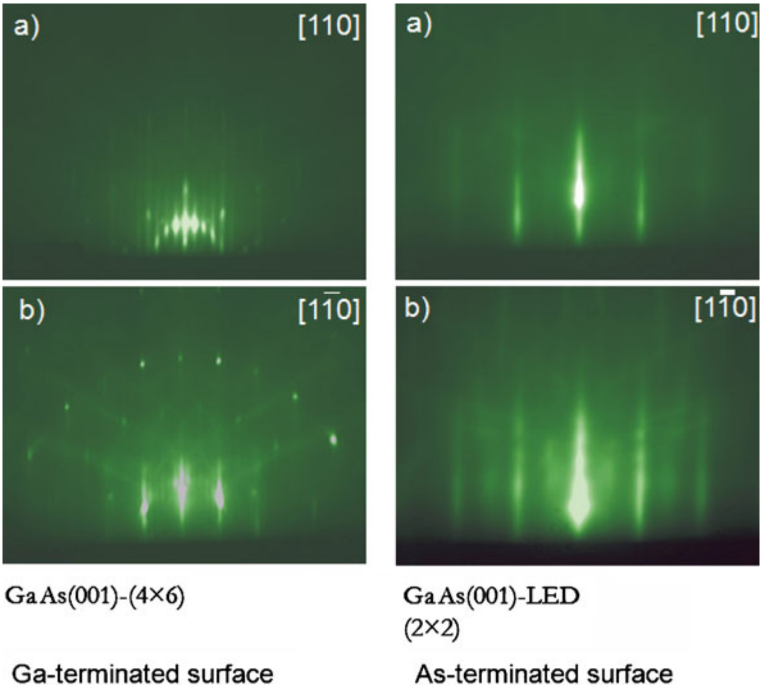

Fig. 17 (*Left*) RHEED images from a clean Ga-terminated GaAs(001) surface showing pseudo-(4 × 6) superstructure reflections. The RHEED beam was along the azimuthal [108] direction of GaAs(001) in **a** and along [1–10] in **b**. (*Right*) RHEED images from a clean As-terminated GaAs(001) surface of a LED structure after desorption of an As-cap layer at 400°C in UHV, showing (2 × 2) superstructure reflections. The RHEED beam was along the azimuthal [108] direction of GaAs(001) in **a** and along [1–10] in **b**. (Electron energy: 15 keV) [112]

The system Fe/GaAs(001) has been widely investigated in literature reports. For instance, magnetic anisotropy is discussed in a recent paper [104], and an extensive review up to the year 2005 is given in Ref. [105]. The advantage of bcc-Fe(001) contacts on GaAs(001) is the high Curie temperature of 1043 K, the high Fe atomic moment of 2.2 μ_B, the high electronic spin polarization at the Fermi energy of 44%, and the favourable lattice parameter which corresponds to a lattice misfit $2a_{Fe}/a_{GaAs}$ of only 1.4%. Another advantage for spin injection is the formation of a natural Schottky barrier at the Fe/GaAs interface, which acts as a natural tunnel barrier and is favourable for electrical spin injection.

However, a problem with Fe/GaAs is the high chemical reactivity of the GaAs surface with respect to Fe. In order to achieve effective spin injection, it is crucial to prepare an optimum crystallographic and magnetic interface structure, because strongly interdiffused, weakly magnetic or non-magnetic Fe-As phases/compounds ("magnetic dead layers") are detrimental for spin injection. High quality epitaxial growth of Fe(001) on the GaAs(001) surface is another crucial condition for spin injection. Our earlier *in situ* CEMS measurements in UHV have demonstrated that epitaxial Fe(001) island growth on GaAs(001) occurs below a critical percolation thickness of ~4 ML Fe, combined with superparamagnetism, while smooth closed Fe(001) films are formed above that critical thickness [106].

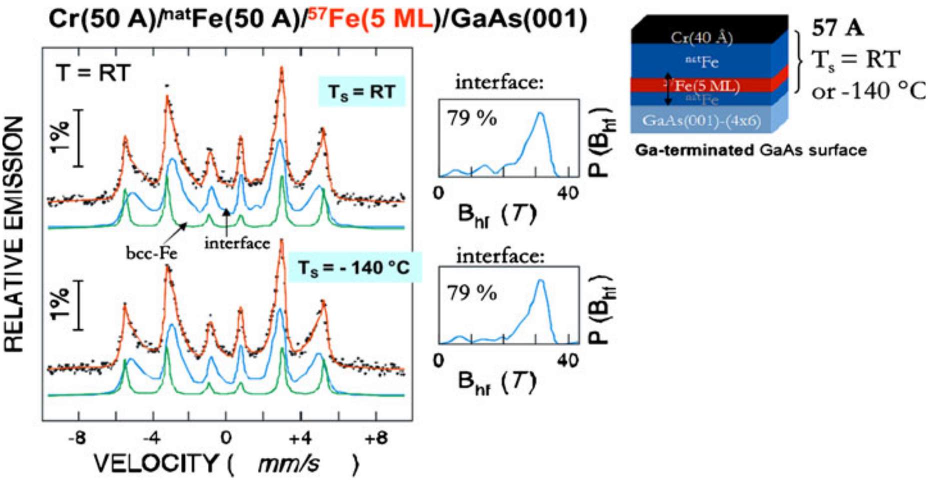

Fig. 18 RT-CEM spectra and corresponding hyperfine-field distributions P(B_{hf}) (*right-hand side*) taken from an epitaxial buried 5-ML-thick ^{57}Fe(001) probe layer placed directly at the Ga-terminated GaAs(001)-(4 × 6) surface. The sample structure was Cr(4 nm)-cap/Fe(5 nm)/^{57}Fe(5 ML)/GaAs(001)-(4 × 6). The natural Fe and ^{57}Fe layers (total thickness: 5.7 nm) were grown on GaAs(001) at room temperature (*top*) and at −140°C (*bottom*), respectively. The incident γ-ray was perpendicular to the film surface [112]

We have employed CEMS and ^{57}Fe probe layers at the Fe/GaAs and Fe/GaAs(001)-LED interface as a standard diagnostic tool for the characterization of the structural and magnetic state of the interface region [107–110]. The substrate surfaces were Ga-terminated in the case of GaAs(001)-(4 × 6) substrates and cleaned in UHV by cycles of Ar^+ sputtering and annealing, following Ref. [111]. Clean As-terminated GaAs(001)-(2 × 2)-LED surfaces were obtained by desorption of a protective As coating layer at 400°C in UHV. Figure 17 shows RHEED patterns of the Ga-terminated (left) and As-terminated (right) surfaces, respectively, indicating clean, well-ordered and atomically smooth surfaces.

Figure 18 shows typical CEM spectra obtained from a 5-ML- (or 0.72-nm-) thick epitaxial ^{57}Fe(001) probe layer (95.5% enriched) placed directly on the Ga-terminated GaAs(001)-(4 × 6) surface, followed by a 5-nm-thick natural Fe(001) layer and a 5-nm Cr(001) cap [112]. The films were grown with the substrate at RT (top spectrum) or at −140°C (bottom spectrum). RHEED indicated epitaxial film growth for both types of samples (not shown). The top spectrum (T_s = RT) was least-squares fitted with two subspectra: (i) a Zeeman sextet with sharp Lorentzian lines, a hyperfine field of 33.0 ± 0.01 T, a quadrupole level shift $2\varepsilon = 0$ mm/s and an isomer shift $\delta = 0$ mm/s, originating predominantly from probe-layer ^{57}Fe atoms in the bcc-Fe phase; (ii) a subspectrum with a hyperfine-field distribution P(B_{hf}), implying an average hyperfine field $B_{hf} = 26.8 \pm 0.2$ T, average $2\varepsilon = -0.03 \pm 0.01$ mm/s and average isomer shift $< \delta > = 0.15 \pm 0.04$ mm/s, which is attributed to ^{57}Fe probe layer atoms affected by the GaAs interface (interface Fe alloy). In-plane Fe spin orientation, i.e. an intensity ratio of $R_{23} = x = 4$ was assumed for the fitting. The relative spectral area of the sharp bcc-Fe sextet is 21% (and 79% for the P(B_{hf})-interface component), as obtained from the fitting. Very similar Mössbauer parameters were obtained from the fitting of the bottom spectrum in Fig. 18 for the sample grown at $T_s = -140°C$. This demonstrates that low-temperature epitaxial Fe(001) growth at −140°C on GaAs(001) leads to the same interface state as Fe film growth at RT. This conclusion is also supported by the similar shape of the $P(B_{hf})$ distributions for film growth at RT and −140°C, Fig. 18 (right-hand side).

The value of the average isomer shift $<\delta>= 0.15 \pm 0.04$ mm/s of the $P(B_{hf})$ spectral component for the film grown at RT (and $<\delta>= 0.11 \pm 0.04$ mm/s for the film grown at −140°C) is found to be slightly positive relative to the value of $\delta = 0$ mm/s of pure bulk α-Fe at RT (our reference absorber). This indicates a decrease of the s-electron density at the ^{57}Fe nucleus at the Fe/GaAs interface. This effect can be explained by interdiffused Ga and/or As neighboring atoms of ^{57}Fe in the bcc-Fe lattice, since positive isomer shifts are typically observed for $Fe_{1-x}Ga_x$ and $Fe_{1-x}As_x$ solid solutions [113, 114].

It is obvious that a minor amount (nominally ∼14%) of the total Mössbauer signal (total spectral area) originates also from ^{57}Fe atoms in the 5-nm-thick natural bcc-Fe(001) layer (of ∼2% in ^{57}Fe isotopic abundance), while 79% of the total signal (the interfacial $P(B_{hf})$ spectral component) can be attributed to an interface alloy in the ^{57}Fe probe layer. The small rest (∼7%) of the signal intensity arises from ^{57}Fe atoms in the bcc-Fe phase existing in the probe layer. A simple calculation shows that effectively a thickness of 0.66 nm (or 4.6 ML) of the ^{57}Fe probe layer is affected by Fe/GaAs interface alloying, and only 0.06 nm (or 0.4 ML) of the probe layer exists in the bcc-Fe phase. This result demonstrates that nearly the entire 5-ML-thick ^{57}Fe probe layer is affected by alloying with Ga and/or As atoms from the substrate. Since also the RT-CEM spectrum of the films deposited at $T_s = -140°C$ (Fig. 18, bottom) exhibits a spectral area of 79% for the interfacial $P(B_{hf})$ component, the effective thickness of the interdiffused interface region apparently is independent of Fe film growth at RT or at −140°C on GaAs(001).

One of the most important results of our study follows from the hyperfine-field distributions $P(B_{hf})$ in Fig. 18. The fact that no significant contribution at $B_{hf} = 0$ T in $P(B_{hf})$ exists proves the absence of a "magnetic dead layer" in the interfacial region of both samples. The average hyperfine field $<B_{hf}>$ at RT in the interfacial region (obtained from $P(B_{hf})$) is 26.8 T for $T_s = RT$ and 27.4 T for $T_s = -140°C$, i.e., about 27 T. Assuming proportionality of hyperfine field and Fe atomic magnetic moment, μ_{Fe}, and the validity of the conversion factor of 15 T/μ_B for Fe alloys [31], we obtain a rather high value μ_{Fe} of ∼1.8 μ_B for the alloyed Fe/GaAs(001) interface region. The peak field B_{hf}^{peak} at the maximum of $P(B_{hf})$ is found to be at 31.2 T for both samples (Fig. 18), corresponding to a calculated Fe atomic moment of 2.1 μ_B. Our μ_{Fe} values, calculated from the measured hyperfine fields, are in good agreement with Fe atomic moments of 1.84–1.96 μ_B measured directly by XMCD on Fe(001) sub-monolayers on GaAs(001) [115]. Such bulk-like high Fe magnetic moments are a crucial condition for spintronics applications via electron spin injection.

Now we come back to the topic of the spin LED. As discussed above, the disadvantage of many published approaches is the requirement of a strong external field of more than 2 T counterbalancing the shape anisotropy of the ferromagnetic thin film contact in order to achieve a perpendicular (vertical) magnetization direction along the optical quantization axis in the so-called Faraday geometry. Therefore, ferromagnetic contacts with spontaneous perpendicular magnetization direction (perpendicular magnetic anisotropy, PMA) are highly desirable, since they

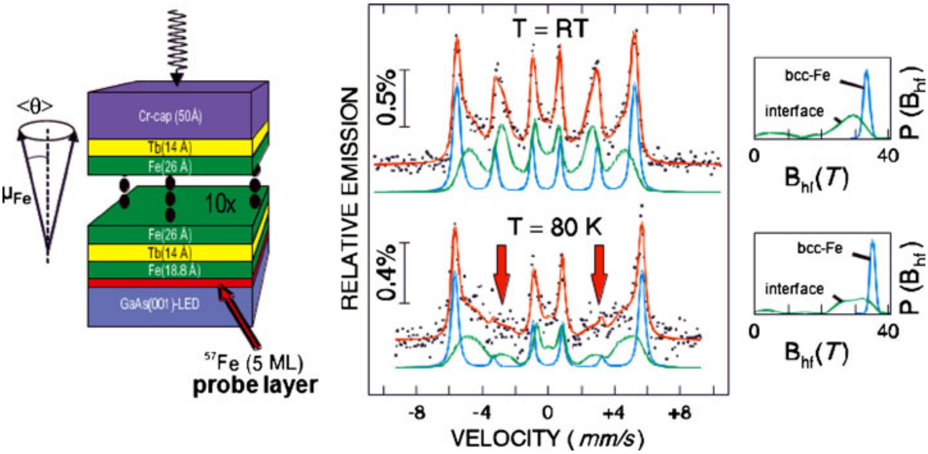

Fig. 19 CEM spectra taken at RT (*top*) and 80 K (*bottom*) from an epitaxial buried 5-ML-thick ^{57}Fe(001) probe layer placed directly at the As- terminated GaAs(001)-(2 × 2) surface of a LED and covered by a Tb/Fe multilayer. The corresponding hyperfine-field distributions P(B_{hf}) are shown on the right-hand side. The sample structure is schematically shown on the left-hand side. The arrows emphasize the nearly disappearance of the lines #2 and 5 at 80 K, indicating perpendicular Fe spin texture in the ^{57}Fe interfacial probe layer. The incident γ-ray was perpendicular to the film plane [112]

allow optical detection of electron spin injection in the remanent state (i.e. at zero external magnetic field). The principle is sketched schematically in Fig. 16 (right).

The successful fabrication and CEMS-characterization of ferromagnetic Fe/Tb multilayer contacts with PMA on the clean As-terminated GaAs(001)–(2 × 2) surface of a GaAs-based LED heterostructure are described in Refs. [109, 110]. It is well known that bcc-Fe layers in nanoscale Fe/Tb multilayers exibit PMA [26, 116–125] due to interface anisotropy. The PMA is conceived to be caused by antiferromagnetically exchange-coupled Fe-Tb atomic pairs combined with single-ion anisotropy and the large orbital moment of the Tb ion [123–125]. An ultrathin amorphous Fe-Tb alloy phase at the Fe/Tb interface (a few atomic layers thick), as observed by Mössbauer spectroscopy [116–121], is also involved in creating PMA. Figure 19 shows CEM spectra taken at RT (top) and 80 K (bottom) from a GaAs(001)-based LED (with an InGaAs quantum well) carrying a Tb/Fe-multilayer electrode and a 5-ML-thick ^{57}Fe(001) probe layer at the interface . The exact composition of the sample is:

$$\left[\text{Fe (2.6nm) /Tb (1.4nm)}\right]_{10}\text{/Fe (1.88nm) /}^{57}\text{Fe (5ML) /GaAs-LED.}$$

The metal contact was grown at RT by MBE on the clean As-terminated GaAs(001)-(2 × 2) surface of the LED (Fig. 16, right panel). The epitaxial 5-ML- (or 0.72-nm-) thick ^{57}Fe(001) probe layer was grown first, followed by 1.88 nm of epitaxial natural Fe(001). Thus, the total Fe(001) thickness is 2.6 nm. Subsequently, a [Fe(2.6 nm)/Tb(1.4 nm)]$_{10}$ multilayer (containing natural Fe) was grown, coated by Cr(5 nm) for protection. The 5-ML ^{57}Fe layer probes the Fe- magnetic state/ Fe-spin structure directly at the Fe/GaAs-LED interface. A schematic drawing

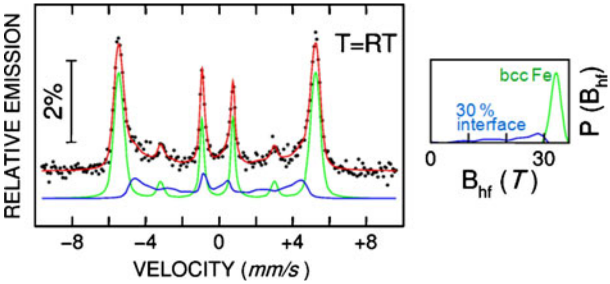

Fig. 20 RT-CEM spectrum and corresponding hyperfine-field distribution P(B_{hf}) (*right-hand side*) from an epitaxial buried 10-ML-thick ^{57}Fe probe layer placed directly at the surface of an epitaxial MgO(001) tunnel barrier on GaAs(001)-(2 × 2)-LED and covered by a [natural-Fe(2.6 nm)/Tb(1.4 nm)] multilayer with perpendicular magnetic anisotropy and a Au cap. The nearly disappearance of the lines #2 and 5 indicates strong perpendicular Fe spin texture in the ^{57}Fe probe layer in contact with MgO(001). The incident γ-ray was perpendicular to the film plane [126]

of the sample structure is shown in Fig. 19 (left-hand side). The CEM spectra in Fig. 19 were again least-squares fitted with two spectral components: (i) a sextet component with a sharp distribution of hyperfine fields P(B_{hf}) (right-hand side) assigned to the bcc-Fe phase, and (ii) a second component with a broad distribution of hyperfine fields, P(B_{hf}), originating from the interfaces in the sample.

The first important observation is that the average hyperfine fields for the bcc-Fe phase obtained from the corresponding distributions in Fig. 19 are $\langle B_{hf}\rangle_{bcc-Fe} = 33.5 \pm 0.1$ T at RT and 35.3 ± 0.4 T at 80 K. These values are slightly enhanced with respect to the bulk α-Fe values because the perpendicular component of the demagnetization field adds to the intrinsic bcc-Fe hyperfine field [118] in the case of PMA. The average hyperfine fields of the interface component deduced from the corresponding distributions are $\langle B_{hf}\rangle_{interface} = 23.8 \pm 0.3$ T at RT and 26.8 ± 1.0 T at 80 K. These values are relatively large, and no indication of a significant "magnetic dead layer" is observed in the distributions P(B_{hf}) of Fig. 19, similar to the case of Fe grown on the Ga-terminated GaAs(001) surface, as described above. However, the present RT value of $<B_{hf}>_{interface}= 23.8$ T is smaller than the corresponding value of $<B_{hf}>_{interface}= 27$ T for the Ga-terminated Fe/GaAs(001) interface at RT. Here, P(B_{hf}) in Fig. 19 should be attributed to the spectral contributions from the alloyed ^{57}Fe/GaAs interface (nominally ~55% contribution) and the alloyed natural-Fe/Tb interfaces (nominally ~45% contribution), which are difficult to distinguish spectroscopically. Using the conversion factor of 15 T/μ_B, an average Fe atomic moment of ~1.6 μ_B can be estimated from the average hyperfine field, averaged over all interfaces involved.

As decribed in Section 3.1, the measured line-intensity ratio R_{23} (=x) in the CEM spectra of Fig. 19 provides information on the canting angle θ (identical to the angle Ψ in Section 3.1) of the Fe magnetic moments μ_{Fe} relative to the film normal direction (Figs. 4 and 19). We use $\langle\cos^2(\theta)\rangle = (4 - R_{23}) / (4 + R_{23})$ in order to calculate the average canting angle $\langle\theta\rangle = \text{arcos}\left[(4 - R_{23}) / (4 + R_{23})\right]^{1/2}$. It is found that at RT $< \theta >_{bcc-Fe}= 39°$ for the bcc-Fe phase and $< \theta >_{interface}= 66°$ for the interface regions. Both values indicate already out-of-plane Fe spin components. The perpendicular components increase at 80 K, where $<\theta>_{\text{bcc}-\text{Fe}} = 22^\circ$ for the bcc-Fe phase and $<\theta>_{\text{interface}} = 33^\circ$ for the interface region. However, since the nominal Mössbauer signal (relative spectral area) from this sample originates to only ~55% from the 5-ML-thick ^{57}Fe probe layer and the rest of 45% from ^{57}Fe in the natural Fe/Tb multilayer, we cannot claim that these canting angles are typical for the 5-ML ^{57}Fe probe layer, because the measurement averages over the whole sample. However, we can give an approximation for the angle $<\theta>_{\text{Fe}}$ of the bcc-Fe phase in the probe layer, since we have measured the canting angle $<\theta>_{\text{Fe/Tb}}$ for the bcc-Fe phase in a reference sample with the same structure as the probe-layer sample, except that all Fe layers were isotopically enriched to 95% in ^{57}Fe. This fully enriched sample showed values of $<\theta>_{\text{Fe/Tb}} = 32^\circ$ at RT and 24° at 80 K, averaged over all the polycrystalline bcc-^{57}Fe layers in the reference sample. Using the relation $\langle\cos^2\theta\rangle_{\text{bcc}-\text{Fe}} = 0.55\,\langle\cos^2\theta\rangle_{\text{Fe}} + 0.45\,\langle\cos^2\theta\rangle_{\text{Fe/Tb}}$, we calculate values of $<\theta>_{\text{Fe}} = 44^\circ$ at RT and $<\theta>_{\text{Fe}} = 20^\circ$ at 80 K for the bcc-Fe phase in the 5-ML ^{57}Fe probe layer [112]. This supports the above conclusion that spontaneous perpendicular Fe spin components exist in the ^{57}Fe probe layer at the Fe/GaAs-LED interface. Recently, a spin LED with an inserted MgO(001) tunnel barrier was developed, which exhibits strong perpendicular Fe spin components even at RT. The CEM spectrum of such a spin LED [126] is displayed in Fig. 20. The 10-ML-thick ^{57}Fe(001) probe layer, deposited onto the MgO(001)/GaAs(001)-LED surface and covered by a Fe/Tb multilayer with PMA, shows a small canting angle $<\theta>$ of only 21° at RT and a large bcc-Fe spectral contribution of ~70%, while the contribution from interface alloying (~30%) is rather small. It was shown by in-field Mössbauer spectroscopy in Ref. [26] that the Fe spins in such Fe/Tb multilayers form a "cone state", with the Fe spins lying on a cone of half-angle $<\theta>$ relative to the film normal direction (or cone symmetry axis).

Therefore, such ferromagnetic Fe/Tb multilayer contacts on LED surfaces are useful for electron spin injection and optical detection of spin injection in the Faraday geometry in zero external field. This has been proven in several reports, in which CEMS was an indispensible tool for characterizing the interfacial perpendicular Fe spin structure in these spin-optoelectronic devices [97, 127–129]. The degree of optical circular polarization achieved at RT was 1.5% at remanence and 4.4% at $\mu_o H = 2$ T [129]. Recently, the concept of using Fe/Tb-multilayer contacts with strong PMA at RT was applied to a new type of GaAs(001)-based LED containing light-emitting InAs quantum dots [130, 131]. Combined measurements at RT of the canting angle $<\theta>$ at the Fe/GaAs-LED interface by ^{57}Fe-probe layer CEMS and of the degree of circular polarization of the EL light in remanence allowed to determine the spin relaxation depth of the injected electrons in the semiconductor [131]. Moreover, the successful fabrication and CEMS characterization of ferromagnetic Fe/Tb multilayer contacts with PMA was also reported for the semiconductor InAs(001) [132].

5 Outlook

50 years after R. L. Mössbauer has been awarded the Nobel prize in physics, the Mössbauer effect continues to be a valuable and often unique method in the field of solid state magnetism. "A Mössbauer spectrum does not lie." A simple Mössbauer

measurement can often prove whether a model inferred from macroscopic magnetic measurement is correct or not.

Figure 1 in Ref. [11] gives a schematic overview of topical subjects in the rapidly evolving fields of spintronics and magnetoelectronics [8, 11]. Besides the familiar control of magnetic devices by external magnetic fields, new and exciting phenomena have been discovered recently, including control by a spin polarized current [133], by electric fields [134–137] or by photonic fields in ultrafast light pulses [11]. Most of these phenomena are observed in nanoscale magnetic systems. The influence of a strong electric field at the interface between a ferromagnetic and a ferroelectric (or insulating) material on the interfacial electronic band structure in the ferromagnet [134–136] might be revealed in the Mössbauer isomer shift and/or hyperfine magnetic field, because both quantities are related to the s-electron density at the ^{57}Fe nucleus. One important aspect of Mössbauer spectroscopy is its sensitivity to chemical ordering processes at the atomic scale in magnetic alloys. Mössbauer spectroscopy can contribute to the characterization and development of Mössbauer-isotope containing chemically ordered thin-film Heusler alloys [6, 23, 24, 28, 29], which are important electron spin injectors, e.g. for GMR, TMR or spin-optoelectronics devices, due to their anticipated huge electronic spin polarization at the Fermi energy. Due to their sensitivity to buried interfaces, CEMS and in particular NRS may contribute to the understanding of electric-field controlled effects in magnetism [134–137]. With the advent of new intense synchrotron light sources with micron or submicron focusing (e.g., PETRA III at DESY), one can conceive novel NRS experiments with spatial resolution for the study of nanomagnetism, and even NRS measurements on monolayers of paramagnetic biomolecules (e.g., Fe-porphyrin molecules) magnetically coupled to ferromagnetic surfaces [138, 139] may become feasible. Such experiments are demanding, because mostly they would require *in situ* NRS measurements under ultrahigh-vacuum (UHV) conditions. Moreover, the method of nuclear resonant inelastic x-ray scattering (NRIXS) of synchrotron radiation, which allows to directly measure the phonon density of states, so far has been seldom used in relation to magnetic phenomena, although changes in the phonon spectrum of FeO (an antiferromagnetic material with a large Fe orbital moment) have been observed and interpreted by magneto-elastic coupling [140]. In the future, it is expected that Mössbauer spectroscopy will participate vigorously in the discovery and understanding of novel phenomena in magnetism at the nanoscale.

Acknowledgements This paper could not have been accomplished without significant contributions by the author's former graduate students in Duisburg: A. Khrenov, R. Peters, B. Roldan Cuenya, B. Sahoo, E. Schuster and F. Stromberg. The author is particularly grateful to U. von Hörsten for his expertise technical and computational support and to C. Antoniak, R. A. Brand, B. Krumme, S. Makarov, A. Warland and C. Weis (all Duisburg) for enlightening discussions. The continuous cooperation and valuable discussions with H. Wende (Duisburg) and J. Kirschner (Halle) are highly appreciated. The author thanks G. Bayreuther (Regensburg and Halle) for critically reading the manuscript and for valuable comments. This work was financially supported by the Deutsche Forschungsgemeinschaft (Sonderforschungsbereich 491 Bochum-Duisburg).

References

1. Blundell, S.: Magnetism in Condensed Matter. Oxford Master Series in Condensed Matter Physics. Oxford University Press, Oxford, New York (2003)
2. Reiff, W.M., Wong, H., Frankel, R.B., Foner, S.: Inorg. Chem. **16**, 1036 (1977)

3. Eibschütz, M., Davidson, G.R., Guggenheim, H.J.: Phys. Rev. B **9**, 3885 (1974)
4. Ito, A., Horiike, M.: J. Phys. (Paris) Colloq. **40**, C2–C290 (1979)
5. Moodera, J.S., Nassar, J., Mathon, G.: Annu. Rev. Mater. Sci. **29**, 381 (1999)
6. Ksenofontov, V., Wojcik, M., Wurmehl, S., Schneider, H., Balke, B., Jakob, G., Felser, C.: J. Appl. Phys. **107**, 09B106 (2010)
7. Zutic, I., Fabian, J., Das Sarma, S.: Rev. Mod. Phys. **76**, 323 (2004)
8. Bader, S.D.: Rev. Mod. Phys. **78**, 1 (2006)
9. Bader, S.D., Buchanan, K.S., Chung, S.-H., Guslienko, K.Y., Hoffmann, A., Li, Y., Novisad, V.: Superlattices Microstruct. **41**, 72 (2007)
10. Zabel, H.: Superlattices Microstruct. **46**, 541 (2009)
11. Bader, S.D., Parkin, S.S.P.: Annu. Rev. Condens. Matter Phys. **1**, 71 (2010)
12. Grünberg, P., Schreiber, R., Pang, Y., Brodsky, M.B., Sowers, H.: Phys. Rev. Lett. **57**, 2442 (1986)
13. Baibich, M.N., Broto, J.M., Fert, A., Nguyen van Dau, F., Petroff, F., Etienne, P., Creuzet, G., Friederich, A., Chazelas, J.: Phys. Rev. Lett. **61**, 2472 (1988)
14. Binasch, G., Grünberg, P., Saurenbach, F., Zinn, W.: Phys. Rev. B **39**, 4828 (1989)
15. Bruno, P.: Phys. Rev. B **49**, 13231 (1994)
16. Zahn, P., Mertig, I., Richter, M., Eschrig, H.: Phys. Rev. Lett. **75**, 2996 (1995)
17. Chappert, J.: Hyperfine Interact. **13**, 25 (1983)
18. Sauer, Ch., Zinn, W.: In: Bennett, L.H., Watson, R.E. (eds.) Magnetic Multilayers. World Scientific, Singapore (1993)
19. Przybylski, M.: Hyperfine Interact. **113**, 135 (1998)
20. Shinjo, T., Keune, W.: J. Magn. Magn. Mater. **200**, 598 (1999)
21. Gerdau, E., de Waard, H. (eds.): Nuclear Resonant Scattering of Synchrotron Radiation. Baltzer Science Publishers, Amsterdam (1999/2000)
22. Dürr, H.A., et al.: IEEE Trans. Magn. **45**, 15 (2009)
23. Makarov, S., Krumme, B., Stromberg, F., Weis, C., Keune, W., Wende, H.: Appl. Phys. Lett. **99**, 141910 (2011)
24. Krumme, B., Weis, C., Herper, H.C., Stromberg, F., Antoniak, C., Warland, A., Schuster, E., Srivastava, P., Walterfang, M., Fauth, K., Minár, J., Ebert, H., Entel, P., Keune, W., Wende, H.: Phys. Rev. B **80**, 144403 (2009)
25. Schmidbauer, E., Keller, M.: J. Magn. Magn. Mater. **297**, 107 (2006)
26. Tappert, J., Neumann, S., Brand, R.A., Keune, W., Klose, F., Maletta, H.: Europhys. Lett. **46**, 238 (1999)
27. Mibu, K., Tanaka, S., Shinjo, T.: J. Phys. Soc. Jpn. **67**, 2633 (1998)
28. Mibu, K., Gondo, D., Hori, T., Tanaka, M.A., Kondou, K., Kasai, S., Ono, T.: J. Phys.: Conf. Ser. **200**, 062012 (2010)
29. Mibu, K., Gondo, D., Hori, T., Ishikawa, Y., Tanaka, M.A.: J. Phys.: Conf. Ser. **217**, 012094 (2010)
30. Preston, R.S., Hanna, S.S., Heberle, J.: Phys. Rev. **128**, 2207 (1962)
31. Gubbens, P.C.M., Buschow, K.H.J.: J. Phys. F **4**, 921 (1974)
32. Hines, W.A., Menotti, A.H., Budnick, J.I., Burch, T.J., Litrenta, T., Niculescu, V., Raj, K.: Phys. Rev. B **13**, 4060 (1976)
33. Liljequist, D., Ekdahl, T., Bäverstam, U.: Nucl. Instrum. Methods **155**, 529 (1978)
34. Keune, W., Schatz, A., Ellerbrock, R.D., Fuest, A., Wilmers, K., Brand, R.A.: J. Appl. Phys. **79**, 4265 (1996)
35. Roldan Cuenya, B., Keune, W., Li, D., Bader, S.D.: Phys. Rev. B **71**, 064409 (2005)
36. Rader, O., Carbone, C., Clemens, W., Vescovo, E., Blügel, S., Eberhardt, W., Gudat, W.: Phys. Rev. B **45**, 13823 (1992)
37. Rader, O., Vescovo, E., Redinger, J., Blügel, S., Carbone, C., Eberhardt, W., Gudat, W.: Phys. Rev. Lett. **72**, 2247 (1994)
38. Vogel, J., Fontaine, A., Cros, V., Petroff, F., Kappler, J.-P., Krill, G., Rogalev, A., Goulon, J.: Phys. Rev. B **55**, 3663 (1997)
39. Klautau, A.B., Peduto, P.R., Frota-Pessoa, S.: J. Magn. Magn. Mater. **186**, 223 (1998)
40. Stoeffler, D., Ounadjela, K., Sticht, J., Gautier, F.: Phys. Rev. B **49**, 299 (1994)
41. Li, M., et al.: J. Phys.: Condens. Matter **6**, L785 (1994)
42. Cheng, L., Altounian, Z., Ryan, D.H., Ström-Olsen, J.O.: J. Appl. Phys. **91**, 7188 (2002)
43. Liu, C., Bader, S.D.: J. Vac. Sci. Technol. A **8**, 2727 (1990)
44. Jin, X.F., Barthel, J., Shen, J., Manoharan, S.S., Kirschner, J.: Phys. Rev. B **60**, 11809 (1999)
45. Li, C., Freeman, A.J., Jansen, H.J.F., Fu, C.L.: Phys. Rev. B **42**, 5433 (1990)

46. Blügel, S., Drittler, B., Zeller, R., Dederichs, P.H.: Appl. Phys. Solid Surf. **49**, 547 (1989)
47. Li, D., Roldan Cuenya, B., Pearson, J., Bader, S.D., Keune, W.: Phys. Rev. B **64**, 144410 (2001)
48. Weber, W., Wesner, D.A., Hartmann, D., Güntherodt, G.: Phys. Rev. B **46**, 6199 (1992)
49. Kiauka, W., van Cuyck, C., Keune, W.: Mater. Sci. Eng. B **12**, 273 (1992)
50. Boeglin, C., Bulou, H., Hommet, J., Le Cann, X., Magnan, H., Le Fevre, P., Chandesris, D.: Phys. Rev. B **60**, 4220 (1999)
51. Wertheim, G.K.: Mössbauer Effect: Principles and Applications. Academic Press, New York (1964)
52. Mühlbauer, H., Müller, Ch, Dumpich, G.: J. Magn. Magn. Mater. **192**, 423 (1999)
53. Le Cann, X., Boeglin, C., Carriere, B., Hricovini, K.: Phys. Rev. B **54**, 373 (1996)
54. Kisters, G., Sauer, Ch., Tsymbal, E., Zinn, W.: Hyperfine Interact. **92**, 1285 (1994)
55. Ohnishi, S., Freeman, A.J., Weinert, M.: Phys. Rev. B **28**, 6741 (1983)
56. Ohnishi, S., Weinert, M., Freeman, A.J.: Phys. Rev. B **30**, 36 (1984)
57. Roldan Cuenya, B., Doi, M., Löbus, S., Courths, R., Keune, W.: Surf. Sci. **493**, 338 (2001)
58. Bader, S.D.: Rev. Mod. Phys. **78**, 1 (2006)
59. Parkin, S.S.P., Hayashi, M., Thomas, L.: Science **320**, 190 (2008)
60. Röhlsberger, R., Thomas, H., Schlage, K., Burkel, E., Leupold, O., Rüffer, R.: Phys. Rev. Lett. **89**, 237201 (2002)
61. Klein, T., Röhlsberger, R., Crisan, O., Schlage, K., Burkel, E.: Thin Solid Films **51**, 52531 (2006)
62. Kuncser, V.E., Doi, M., Keune, W., Askin, M., Spies, H., Jiang, J.S., Inomata, A., Bader, S.D.: Phys. Rev. B **68**, 064416 (2003)
63. Fullerton, E.E., Jiang, J.S., Bader, S.D.: J. Magn. Magn. Mater. **200**, 392 (1999)
64. Choi, Y., Jiang, J.S., Ding, Y., Rosenberg, R.A., Pearson, J.E., Bader, S.D., Zambano, A., Murakami, M., Takeuchi, I., Wang, Z.L., Liu, J.P.: Phys. Rev. B **75**, 104432 (2007)
65. The (Sm-Co)/Fe samples were prepared by J. S. Jiang, Materials Science Division, Argonne National Laboratory, Argonne, IL 60439, U.S.A.
66. Fullerton, E.E., Jiang, J.S., Grimsditch, M., Sowers, C.H., Bader, S.D.: Phys. Rev. B **58**, 12193 (1998)
67. Mibu, K., Nagahama, T., Shinjo, T.: J. Magn. Magn. Mater. **163**, 75 (1996)
68. Chumakov, D., Schäfer, R., Elefant, D., Eckert, D., Schultz, L., Yan, S.S., Barnard, J.A.: Phys. Rev. B **66**, 134409 (2002)
69. Kuncser, V., Keune, W., Vopsaroiu, M., Bissell, P.R.: Nucl. Instrum. Methods Phys. Res. B **245**, 539 (2006)
70. Kuncser, V., Keune, W.: J. Magn. Magn. Mater. **323**, 2196 (2011)
71. Brand, R.A.: Nucl. Instrum. Methods Phys. Res. **28**, 417 (1987)
72. Uzdin, V.M., Vega, A.: Nanotechnology **19**, 315401 (2008); Phys. Rev. B **77**, 134446 (2008)
73. Uzdin, V.M., Vega, A., Khrenov, A., Keune, W., Kuncser, V.E., Jiang, J.S., Bader, S.D.: Phys. Rev. B **85**, 024409 (2012)
74. Nogués, J., Schuller, I.K.: J. Magn. Magn. Mater. **192**, 203 (1999)
75. Stromberg, F.: Dissertation, Universität Duisburg-Essen (2009, in German)
76. Kuncser, V., Doi, M., Sahoo, B., Stromberg, F., Keune, W.: J. Appl. Phys. **94**, 3573 (2003)
77. Kuncser, V.E., Stromberg, F., Acet, M., Keune, W.: J. Appl. Phys. **97**, 063513 (2005)
78. Stromberg, F., Keune, W., Kuncser, V., Westerholt, K.: Phys. Rev. B **72**, 064440 (2005)
79. Radu, F., Zabel, H.: In: Bader, S.D., Zabel, H. (eds.) Magnetic Heterostructures, Advances and Perspectives in Spinstructures and Spintransport. Springer, Berlin (2007)
80. Schulthess, T.C., Butler, W.H.: Phys. Rev. Lett. **81**, 4516 (1998); J. Appl. Phys. **85**, 5510 (1999)
81. Stamps, R.L.: J. Phys. D **33**, R247 (2000)
82. Krivorotov, I.N., Leighton, C., Nogués, J., Schuller, I.K., Dahlberg, E.D.: Phys. Rev. B **68**, 054430 (2003)
83. Kiwi, M.: J. Magn. Magn. Mater. **234**, 584 (2001)
84. Kiwi, M., Mejia-Lopez, J., Portugal, R.D., Ramirez, R.: Europhys. Lett. **48**, 573 (1999)
85. Morales, R., Li, Z.-P., Petracic, O., Batlle, X., Schuller, I.K., Olamit, J., Liu, K.: Appl. Phys. Lett. **89**, 072504 (2006)
86. Macedo, W.A.A., Sahoo, B., Kuncser, V., Eisenmenger, J., Felner, I., Nogués, J., Liu, K., Keune, W., Schuller, I.K.: Phys. Rev. B **70**, 224414 (2004)
87. Sahoo, B., Macedo, W.A.A., Keune, W., Kuncser, V., Eisenmenger, J., Nogués, J., Schuller, I.K., Felner, I., Liu, K., Röhlsberger, R.: Hyperfine Interact. **169**, 1371 (2006)

88. Macedo, W.A.A., Sahoo, B., Eisenmenger, J., Martins, M.D., Keune, W., Kuncser, V., Röhlsberger, R., Leupold, O., Rüffer, R., Nogués, J., Liu, K., Schlage, K., Schuller, I.K.: Phys. Rev. B **78**, 224401 (2008)
89. Sturhahn, W.: Hyperfine Interact. **125**, 149 (2000)
90. Prinz, G.A.: Science **250**, 1092 (1990)
91. Fiederling, R., Keim, M., Reuscher, G., Ossau, W., Schmidt, G., Waag, A., Molenkamp, L.W.: Nature (London) **402**, 787 (1999)
92. Wolf, S.A., Awschalom, D.D., Buhrman, R.A., Daughton, J.M., von Molnar, S., Roukes, M.L., Chtchelkanova, A.Y., Treger, D.M.: Science **294**, 1488 (2001)
93. Žutić, I., Fabian, J., das Sarma, S.: Rev. Mod. Phys. **76**, 323 (2004)
94. Hanbicki, A.T., Jonker, B.T., Itskos, G., Kioseoglou, G., Petrou, A.: Appl. Phys. Lett. **80**, 1240 (2002)
95. Zhu, H.J., Ramsteiner, M., Kostial, H., Wassermeier, M., Schönherr, H.-P., Ploog, K.H.: Phys. Rev. Lett. **87**, 016601 (2001)
96. Jiang, X., Wang, R., Shelby, R.M., MacFarlane, R.M., Bank, S.R., Harris, J.S., Parkin, S.S.P.: Phys. Rev. Lett. **94**, 056601 (2005)
97. Gerhardt, N.C., Hövel, S., Brenner, C., Hofmann, R.M., Lo, F.-Y., Reuter, D., Wieck, A.D., Schuster, E., Keune, W., Westerholt, K.: Appl. Phys. Lett. **87**, 032502 (2005)
98. Kioseoglou, G., Yasar, M., Li, C.H., Korkusinski, M., Diaz-Avila, M., Hanbicki, A.T., Hawrylak, P., Petrou, A., Jonker, B.T.: Phys. Rev. Lett. **101**, 227203 (2008)
99. Wu, M.W., Jiang, J.H., Weng, M.Q.: Phys. Rep. **493**, 61 (2010)
100. Li, M.Y., Jähme, H., Soldat, H., Gerhardt, N.C., Hofmann, M.R., Ackemann, T.: Appl. Phys. Lett. **97**, 191114 (2010)
101. Meier, F., Zakharchenya, B.P. (eds.): Optical Orientation. North-Holland, New York (1984)
102. Holub, M., Shin, J., Saha, D., Bhattacharya, P.: Phys. Rev. Lett. **98**, 146603 (2007)
103. Hövel, S., Bischoff, A., Gerhardt, N.C., Hofmann, M.R., Ackemann, T., Kroner, A., Michalzik, R.: Appl. Phys. Lett. **92**, 041118 (2008)
104. Kardasz, B., Mosendz, O., Heinrich, B., Przybylski, M., Kirschner, J.: J. Phys.: Conf. Ser. **200**, 072046 (2010)
105. Wastlbauer, G., Bland, J.A.C.: Adv. Phys. **54** (2005)
106. Roldan Cuenya, B., Naitabdi, A., Schuster, E., Peters, R., Doi, M., Keune, W.: Phys. Rev. B **76**, 094403 (2007)
107. Doi, M., Roldan Cuenya, B., Keune, W., Schmitte, T., Nefedov, A., Zabel, H., Spoddig, D., Meckenstock, R., Pelzl, J.: J. Magn. Magn. Mater. **240**, 407 (2002)
108. Roldan Cuenya, B., Doi, M., Keune, W., Hoch, S., Reuter, D., Wieck, A., Schmitte, T., Zabel, H.: Appl. Phys. Lett. **82**, 1072 (2003)
109. Schuster, E., Keune, W., Lo, F.-Y., Reuter, D., Wieck, A., Westerholt, K.: Superlattices Microstruct. **37**, 313 (2005)
110. Schuster, E., Brand, R.A., Stromberg, F., Lo, F.-Y., Ludwig, A., Reuter, D., Wieck, A.D., Hövel, S., Gerhardt, N.C., Hofmann, M.R., Wende, H., Keune, W.: J. Appl. Phys. **108**, 063902 (2010)
111. Zölfl, M., Brockmann, M., Köhler, M., Keuzer, S., Schweinböck, T., Miethaner, S., Bensch, F., Bayreuther, G.: J. Magn. Magn. Mater. **175**, 16 (1997)
112. Schuster, E.: Dissertation, Universität Duisburg-Essen (2007, in German)
113. Newkirk, L.R., Tsuei, C.C.: Phys. Rev. B **4**, 4046 (1971)
114. Vincze, I., Aldred, A.T.: Phys. Rev. B **9**, 3845 (1974)
115. Claydon, J.S., Xu, Y.B., Tselepi, M., Bland, J.A.C., van der Laan, G.: Phys. Rev. Lett. **93**, 037206 (2004)
116. Cherifi, K., Dufour, C., Piecuch, M., Bruson, A., Bauer, Ph., Marchal, G., Mangin, Ph.: J. Magn. Magn. Mater. **93**, 609 (1991)
117. Mibu, K., Hosoito, N., Shinjo, T.: Hyperfine Interact. **68**, 341 (1991)
118. Scholz, B., Brand, R.A., Keune, W.: Phys. Rev. B **50**, 2537 (1994)
119. Kim, W.S., Kleemann, W., Brand, R.A., Keune, W.: J. Phys., Condens. Matter **11**, 4317 (1999)
120. Tappert, J., Neumann, S., Jungermann, J., Kim, W.S., Ruckert, T., Brand, R.A., Keune, W., Kleemann, W., Richomme, F., Teillet, J., Klose, F., Maletta, H.: Philos. Mag. **80**, 257 (2000)
121. Richomme, F., Teillet, J., Fnidiki, A., Keune, W.: Phys. Rev. B **64**, 094415 (2001)
122. Honda, S., Nawate, M.: J. Magn. Magn. Mater. **136**, 163 (1994)
123. Sato, N.: J. Appl. Phys. **59**, 2514 (1986)
124. Baczewski, L.T., Piecuch, M., Durand, J., Marchal, G., Delcroix, P.: Phys. Rev. B **40**, 11237 (1989)

125. Shan, Z.S., Sellmyer, D.J.: In: Gschneider, K.A., Eyring, L. (eds.) Handbook on the Physics and Chemistry of Rare Earths. Elsevier Science, Amsterdam (1996)
126. The Au/[Fe/Tb]$_4$/^{57}Fe(10ML)/Mg0(001) multilayer was grown on a GaAs(001)-LED and the CEM spectrum was taken by F. Stromberg, University of Duisburg - Essen
127. Gerhardt, N.C., Hövel, S., Brenner, C., Hofmann, M.R., Lo, F.-Y., Reuter, D., Wieck, A.D., Schuster, E., Keune, W., Halm, S., Bacher, G., Westerholt, K.: J. Appl. Phys. **99**, 073907 (2006)
128. Hövel, S., Gerhardt, N.C., Hofmann, M.R., Lo, F.-Y., Reuter, D., Wieck, A.D., Schuster, E., Keune, W., Wende, H., Petracic, O., Westerholt, K.: Appl. Phys. Lett. **92**, 242102 (2008)
129. Hövel, S., Gerhardt, N.C., Hofmann, M.R., Lo, F.-Y., Ludwig, A., Reuter, D., Wieck, A.D., Schuster, E., Wende, H., Keune, W., Petracic, O., Westerholt, K.: Appl. Phys. Lett. **93**, 021117 (2008)
130. Ludwig, A., Roescu, R., Rai, A.K., Trunov, K., Stromberg, F., Li, M., Soldat, H., Ebbing, A., Gerhardt, N.C., Hofmann, M.R., Wende, H., Keune, W., Reuter, D., Wieck, A.D.: J. Cryst. Growth **323**, 376 (2011)
131. Soldat, H., Li, M., Gerhardt, N.C., Hofmann, M.R., Ludwig, A., Ebbing, A., Reuter, D., Wieck, A.D., Stromberg, F., Keune, W., Wende, H.: Appl. Phys. Lett. **99**, 051102 (2011)
132. Peters, R., Keune, W., Schuster, E., Kashiwada, S., Ferhat, M., Yoh, K.: Superlattice. Microstruct. **41**, 81 (2007)
133. Sbiaa, R., Law, R., Lua, S.Y.H., Tan, E.L., Tahmasebi, T., Wang, C.C., Piramanayagam, S.N.: Appl. Phys. Lett. **99**, 092506 (2011)
134. Duan, C.-G., Jaswal, S.S., Tsymbal, E.Y.: Phys. Rev. Lett. **97**, 047201 (2006)
135. Maruyama, T., Shiota, Y., Nozaki, T., Ohta, K., Toda, N., Mizuguchi, M., Tulapurka, A.A., Shinjo, T., Shiraishi, M., Mizukami, S., Ando, Y., Suzuki, Y.: Nature Nanotechnology **4**, 158 (2009)
136. Nozaki, T., Shiota, Y., Shiraishi, M., Shinjo, T., Suzuki, Y.: Appl. Phys. Lett. **96**, 022506 (2010)
137. Kleemann, W.: Physics **2**, 105 (2009)
138. Bernien, M., Miguel, J., Weis, C., Ali, Md.E., Kurde, J., Krumme, B., Panchmatia, P.M., Sanyal, B., Piantek, M., Srivastava, P., Baberschke, K., Oppeneer, P.M., Eriksson, O., Kuch, W., Wende, H.: Phys. Rev. Lett. **102**, 047202 (2009)
139. Wende, H.: Adv. Solid State Phys. **48**, 199 (2009)
140. Struzhkin, V.V., Mao, H.-K., Hu, J., Schwoerer-Böhning, M., Shu, J., Hemley, R.J., Sturhahn, W., Hu, M., Alp, E.E.: Phys. Rev. Lett. **25**, 255501 (2001)